

Molecular Gas in NUClei of GALaxies (NUGA)

XIV. The barred LINER/Seyfert 2 galaxy NGC 3627 [★]

V. Casasola^{1,2}, L.K. Hunt¹, F. Combes³, S. García-Burillo⁴, and R. Neri⁵

¹ INAF-Osservatorio Astrofisico di Arcetri, Largo E. Fermi, 5, 50125 Firenze, Italy

² INAF-Istituto di Radioastronomia, via Gobetti 101, 40129 Bologna, Italy

³ Observatoire de Paris, LERMA, 61 Av. de l'Observatoire, F-75014, Paris, France

⁴ Observatorio Astronómico Nacional (OAN) - Observatorio de Madrid, C/ Alfonso XII, 3, 28014 Madrid, Spain

⁵ IRAM-Institut de Radio Astronomie Millimétrique, 300 Rue de la Piscine, 38406-St.Mt.d'Hères, France

Received ; accepted

Abstract. We present $^{12}\text{CO}(1-0)$ and $^{12}\text{CO}(2-1)$ maps of the interacting barred LINER/Seyfert 2 galaxy NGC 3627 obtained with the IRAM interferometer at resolutions of $2''.1 \times 1''.3$ and $0''.9 \times 0''.6$, respectively. We also present single-dish IRAM 30 m $^{12}\text{CO}(1-0)$ and $^{12}\text{CO}(2-1)$ observations used to compute short spacings and complete interferometric measurements. These observations are complemented by IRAM 30 m measurements of HCN(1–0) emission detected in the center of NGC 3627. The molecular gas emission shows a nuclear peak, an elongated bar-like structure of $\sim 18''$ (~ 900 pc) diameter in both ^{12}CO maps and, in $^{12}\text{CO}(1-0)$, a two-arm spiral feature from $r \sim 9''$ (~ 450 pc) to $r \sim 16''$ (~ 800 pc). The inner $\sim 18''$ bar-like structure, with a north/south orientation (PA = 14°), forms two peaks at the extremes of this elongated emission region. The kinematics of the inner molecular gas shows signatures of non-circular motions associated both with the $18''$ bar-like structure and the spiral feature detected beyond it. The $1.6 \mu\text{m}$ *H*-band 2MASS image of NGC 3627 shows a stellar bar with a PA = -21° , different from the PA (= 14°) of the ^{12}CO bar-like structure, indicating that the gas is leading the stellar bar. The far-infrared *Spitzer*-MIPS 70 and $160 \mu\text{m}$ images of NGC 3627 show that the dust emission is intensified at the nucleus and at the ansae at the ends of the bar, coinciding with the ^{12}CO peaks. The *GALEX* far-ultraviolet (FUV) morphology of NGC 3627 displays an inner elongated (north/south) ring delimiting a hole around the nucleus, and the ^{12}CO bar-like structure is contained in the hole observed in the FUV. The torques computed with the *HST*-NICMOS F160W image and our PdBI maps are negative down to the resolution limit of our images, ~ 60 pc in $^{12}\text{CO}(2-1)$. If the bar ends at ~ 3 kpc, coincident with corotation (CR), the torques are negative between the CR of the bar and the nucleus, down to the resolution limit of our observations. This scenario is compatible with a recently-formed rapidly rotating bar which has had insufficient time to slow down because of secular evolution, and thus has not yet formed an inner Lindblad resonance (ILR). The presence of molecular gas inside the CR of the primary bar, where we expect that the ILR will form, makes NGC 3627 a potential *smoking gun* of inner gas inflow. The gas is fueling the central region, and in a second step could fuel directly the active nucleus.

Key words. galaxies: individual: NGC 3627 – galaxies: spiral – galaxies: active – galaxies: nuclei – galaxies: ISM – galaxies: kinematics and dynamics

1. Introduction

The Nuclei of Galaxies (NUGA) project (García-Burillo et al. 2003) is an IRAM Plateau de Bure Interferometer (PdBI) and 30 m single-dish survey of nearby low-luminosity active galactic nuclei (LLAGN). The aim is to map, at high resolution ($\sim 0''.5$ – $2''$) and high sensitivity (~ 2 – 4 mJy beam $^{-1}$), the distribution and dynamics of the molecular gas in the inner kpc of

the galaxies of our sample, and to study the different mechanisms for gas fueling of LLAGN.

NUGA galaxies analyzed so far show that there is no unique circumnuclear molecular gas feature linked with nuclear activity, but rather a variety of molecular gas morphologies which characterize the inner kpc of active galaxies. We have found one- and two-armed instabilities (García-Burillo et al. 2003), well-ordered rings and nuclear spirals (Combes et al. 2004; Casasola et al. 2008a), circumnuclear asymmetries (Krips et al. 2005), large-scale bars (Boone et al. 2007; Hunt et al. 2008), and smooth disks (Casasola et al. 2010). Among these morphologies, analyzing the torques exerted by the stellar gravitational potential

Send offprint requests to: casasola@ira.inaf.it

[★] Based on observations carried out with the IRAM Plateau de Bure Interferometer. IRAM is supported by the INSU/CNRS (France), MPG (Germany), and IGN (Spain).

on the molecular gas shows that only four NUGA galaxies: NGC 6574 (Lindt-Krieg et al. 2008), NGC 2782 (Hunt et al. 2008), NGC 3147 (Casasola et al. 2008a), and NGC 4579 (García-Burillo et al. 2009) show evidence for gas inflow. These galaxies have several features in common: (1) a large circumnuclear mass concentration (i.e., a dominant stellar bulge); (2) a high circumnuclear molecular gas fraction ($\geq 10\%$); and (3) kinematically decoupled bars with overlapping dynamical resonances. The large amount of gas around the nucleus, combined with dynamical features that enable the gas to penetrate the inner Lindblad Resonance (ILR), seem to be necessary (and perhaps sufficient) ingredients for inducing gas inflow in circumnuclear scales.

The existence of different nuclear molecular morphologies can be sought in the variety of timescales characterizing nuclear activity. Strong fueling only lasts for a time of $t_{\text{fuel}} \sim 0.002 \times t_H$, where $t_H \sim 1.4 \times 10^{10}$ yr is the age of the Universe (Heckman et al. 2004). Thus, the total time during which strong fueling can occur is around $t_{\text{fuel}} \sim 3 \times 10^7$ yr; if there are N fueling events per black hole per Hubble time, each event would have a duration of $t_{\text{event}} \sim 3 \times 10^7/N$ yr. This implies that the strong accretion phase is a fraction $\approx 0.3/N$ of the characteristic galaxy dynamical time ($\sim 10^8$ yr). Although large-scale bars can produce gas inflow (e.g., Combes & Gerin 1985; Sakamoto et al. 1999) and in some cases also drive powerful starbursts (e.g., Knapen et al. 2002; Jogee et al. 2005), a correlation between large-scale bars and nuclear activity has not yet been verified (e.g., Mulchaey & Regan 1997). This lack of correlation is probably related to the different timescales for bar-induced gas inflow (≥ 300 Myr, Jogee et al. 2005), AGN duty cycles ($\sim 10^7$ yr), and intermittent active accretion every $\sim 10^8$ yr (Ferrarese et al. 2001; Marecki et al. 2003; Janiuk et al. 2004; Hopkins & Hernquist 2006; King & Pringle 2007). The comparison of these different timescales suggests that most AGN are in an intermediate phase between active accretion episodes making the detection of galaxies with nuclear accretion somewhat difficult.

Gravitational torques act on timescales of $\sim 10^{6-7}$ yr and are the most efficient mechanism in driving the gas from large spatial scales (some tens of kpc) to intermediate spatial scales (a few hundreds of pc). Dynamical friction and viscous torques are often invoked, in addition to gravitational torques, as possible mechanisms of AGN fueling. However, dynamical friction of giant molecular clouds in the stellar bulge of a galaxy tends to be a slow, inefficient process which, to first approximation, can be neglected relative to gravity torques (García-Burillo et al. 2005). Viscous torques can be more effective, and are favored in the presence of large density gradients and high galactic shear (see García-Burillo et al. 2005, for details). Nevertheless, they are relatively inefficient when there are strong (positive) gravity torques.

This paper is dedicated to the galaxy NGC 3627, the eleventh object of the core NUGA sample studied on a case-by-case basis. NGC 3627 (Messier 66, $D = 10.2$ Mpc, $H_0 = 73$ km s $^{-1}$ Mpc $^{-1}$) is an interacting (e.g., Casasola et al. 2004) and barred galaxy classified as SAB(s)b showing signatures of

Table 1. Fundamental parameters for NGC 3627.

Parameter	Value ^b	Reference ^c
α_{J2000} ^a	11 ^h 20 ^m 15.02 ^s	(1)
δ_{J2000} ^a	12°59′29″50	(1)
V_{hel}	744 km s $^{-1}$	(1)
RC3 Type	SAB(s)b	(2)
Nuclear Activity	LINER/Seyfert 2	(3)
Inclination	61°3	(1)
Position Angle	178° \pm 1°	(1)
Distance	10.2 Mpc (1″ = 49 pc)	(2)
L_B	$4.2 \times 10^{10} L_{\odot}$	(4)
M_{HI}	$8.1 \times 10^8 M_{\odot}$	(5)
M_{H_2}	$4.1 \times 10^9 M_{\odot}$	(6)
M_{dust} (60 and 100 μ m)	$4.5 \times 10^6 M_{\odot}$	(4)
L_{FIR}	$1.2 \times 10^{10} L_{\odot}$	(7)

^a (α_{J2000} , δ_{J2000}) is the phase tracking center of our ^{12}CO interferometric observations, assumed coincident with the dynamical center of NGC 3627 (see Sect. 4.1).

^b Luminosity and mass values extracted from the literature have been scaled to the distance of $D = 10.2$ Mpc.

^c (1) This paper; (2) NASA/IPAC Extragalactic Database (NED, <http://nedwww.ipac.caltech.edu/>); (3) Ho et al. (1997); (4) Casasola et al. (2004); (5) Haan et al. (2008); (6) Kuno et al. (2007); (7) *IRAS* Catalog.

a LINER/Seyfert 2 type nuclear activity (Ho et al. 1997). With NGC 3623 and NGC 3628, it forms the well-known Leo Triplet (M 66 Group, VV 308). Since the discovery of a long plume in H α extending about 50′ to the east of NGC 3628 (Zwicky 1956; Haynes et al. 1979), evidence of past interactions between NGC 3627 and NGC 3628 (the two largest spirals in the group), the Leo Triplet has been extensively studied from the radio to the optical, and in X-ray bandpasses. Optical broadband images of NGC 3627 reveal a pronounced and asymmetric spiral pattern with heavy dust lanes, indicating strong density wave action (Ptak et al. 2006). While the western arm is accompanied by weak traces of star formation (SF) visible in H α , the eastern arm contains a star-forming segment in its inner part (Smith et al. 1994). NGC 3627 also possesses X-ray properties of a galaxy with a recent starburst (Dahlem et al. 1996). Both the radio continuum (2.8 cm and 20 cm) and the $^{12}\text{CO}(1-0)$ emissions show a nuclear peak, extend along the leading edges of the bar forming two broad maxima at the bar ends, and then the spiral arms trail off from the bar ends (Haan et al. 2008; Paladino et al. 2008; Haan et al. 2009). On the contrary, the H α emission exhibits a spiral morphology without signatures of a bar in the atomic gas (Haan et al. 2008; Walter et al. 2008; Haan et al. 2009).

The most recent H α mass determination for NGC 3627 has been obtained by Haan et al. (2008), $M_{\text{HI}} = 8.1 \times 10^8 M_{\odot}$ (reported to our adopted distance of $D = 10.2$ Mpc), on average less than the typical value expected for interacting galaxies of the same Hubble type (Casasola et al. 2004). The H_2 mass con-

Table 2. $^{12}\text{CO}(1-0)$ flux values, both obtained by our observations and extracted from the literature, for NGC 3627.

Reference	Telescope	Diameter [m]	Primary beam or FOV ^a [']	Beam ['' × '']	Flux [Jy km s ⁻¹]
Young et al. (1995)	FCRAO	14	45		786
This paper	PdBI+30 m		42	2.1 × 1.3	668
This paper	PdBI+30 m		22 ^b	2.1 × 1.3	359
This paper	PdBI		22 ^b	2.0 × 1.3	251
This paper	30 m	30	22 (central position)		343 ^c
Helper et al. (2003)	NRAO	12	55 (inner 50'' × 50'')		1100–1200
This paper	30 m	30	22 (inner 50'' × 50'')		1097 ^d

^a Primary beam is considered for single-dish observations, while field-of-view (FOV) for interferometric or combined (interferometric+single-dish) ones.

^b The photometry has been performed within 22'', the $^{12}\text{CO}(1-0)$ primary beam for the 30 m telescope.

^c The $^{12}\text{CO}(1-0)$ recovered flux for the central position (0'', 0'').

^d The $^{12}\text{CO}(1-0)$ recovered flux for inner $\sim 50'' \times 50''$, 5×5 mapping with 7'' spacing (see Sect. 2.2).

tent estimated by Kuno et al. (2007) is $4.1 \times 10^9 M_{\odot}$ (scaled to our distance of $D = 10.2$ Mpc for NGC 3627).

These H_2 and H I mass values give a $\text{H}_2/\text{H I}$ mass ratio of 5.1, high compared to the average ratio expected for galaxies similar to NGC 3627, $M_{\text{H}_2}/M_{\text{H I}} = 0.9$ (Casasola et al. 2004). The high $\text{H}_2/\text{H I}$ mass ratio in NGC 3627 is probably due to the tidal interaction with NGC 3628, since this galaxy has “captured” much of the H I in NGC 3627 (Zhang et al. 1993).

Other molecular transitions have been detected in NGC 3627, including $\text{HCN}(1-0)$, $\text{HCN}(2-1)$, $\text{HCN}(3-2)$, $\text{HCO}^+(1-0)$, and $\text{HCO}^+(3-2)$, suggesting the presence of high density gas (Gao & Solomon 2004; Krips et al. 2008). We list in Table 1 the main observational parameters of NGC 3627.

The structure of this paper is as follows. In Sect. 2, we describe our new observations of NGC 3627 and the literature data with which we compare them. In Sects. 3 and 4, we present the observational results, both single-dish and interferometric, describing morphology, excitation conditions, and kinematics of the molecular gas in the inner kpc of NGC 3627. Comparisons between ^{12}CO observations and those obtained at other wavelengths are given in Sect. 5. In Sect. 6, we describe the computation of the gravity torques derived from the stellar potential in the inner region of NGC 3627, and in Sect. 7, we give an dynamical interpretation of the results. Finally, Sect. 8 summarizes our main results.

We assume a distance to NGC 3627 of $D = 10.2$ Mpc, (HyperLeda DataBase¹) and a Hubble constant $H_0 = 73 \text{ km s}^{-1} \text{ Mpc}^{-1}$. This distance means that 1'' corresponds to 49 pc.

2. Observations

2.1. Interferometric observations

We observed NGC 3627 with the IRAM PdBI (6 antennas) in the ABCD configuration of the array between 2003 September and 2004 February in the $^{12}\text{CO}(1-0)$ [115 GHz] and the $^{12}\text{CO}(2-1)$ [230 GHz] line. The PdBI receiver characteristics, the observing procedures, and the image reconstruction are similar to those described in García-Burillo et al. (2003). The quasar 3C454.3 was used for bandpass calibration, 3C273 for flux calibration, and 1546+027 for phase and amplitude calibrations.

Data cubes with 512×512 pixels ($0''.27 \text{ pixel}^{-1}$ for $^{12}\text{CO}(1-0)$ and $0''.13 \text{ pixel}^{-1}$ for $^{12}\text{CO}(2-1)$) were created over a velocity interval of -242.5 km s^{-1} to $+242.5 \text{ km s}^{-1}$ in bins of 5 km s^{-1} . The images presented here were reconstructed using the standard IRAM/GILDAS² software (Guilloteau & Lucas 2000) and restored with Gaussian beams of dimensions $2''.0 \times 1''.3$ (PA = 23°) at 115 GHz and $0''.9 \times 0''.6$ (PA = 28°) at 230 GHz. We used natural and uniform weightings to generate $^{12}\text{CO}(1-0)$ and $^{12}\text{CO}(2-1)$ maps, respectively. This allows to maximize the flux recovered in $^{12}\text{CO}(1-0)$ and optimize the spatial resolution in $^{12}\text{CO}(2-1)$. In the cleaned maps, the *rms* levels are $3.7 \text{ mJy beam}^{-1}$ and $6.7 \text{ mJy beam}^{-1}$ for the $^{12}\text{CO}(1-0)$ and $^{12}\text{CO}(2-1)$ lines, respectively at a velocity resolution of 5 km s^{-1} . At a level of 3σ no 3 mm (1 mm) continuum was detected toward NGC 3627 down to an *rms* noise level of $0.34 \text{ mJy beam}^{-1}$ ($0.48 \text{ mJy beam}^{-1}$). The conversion factors between intensity and brightness temperature are $34 \text{ K (Jy beam}^{-1})^{-1}$ at 115 GHz and $41 \text{ K (Jy beam}^{-1})^{-1}$ at 230 GHz. All velocities are referred to the systemic velocity $V_{\text{sys, hel}} = 744 \text{ km s}^{-1}$ and $(\Delta\alpha, \Delta\delta)$ offsets are relative to the phase tracking center of our observations ($11^h 20^m 15.02^s$, $12^\circ 59' 29.50''$) [see later Sect. 4.1]. All maps are centered on

¹ Paturel et al. (2003), <http://leda.univ-lyon1.fr>

² <http://www.iram.fr/IRAMFR/GILDAS/>

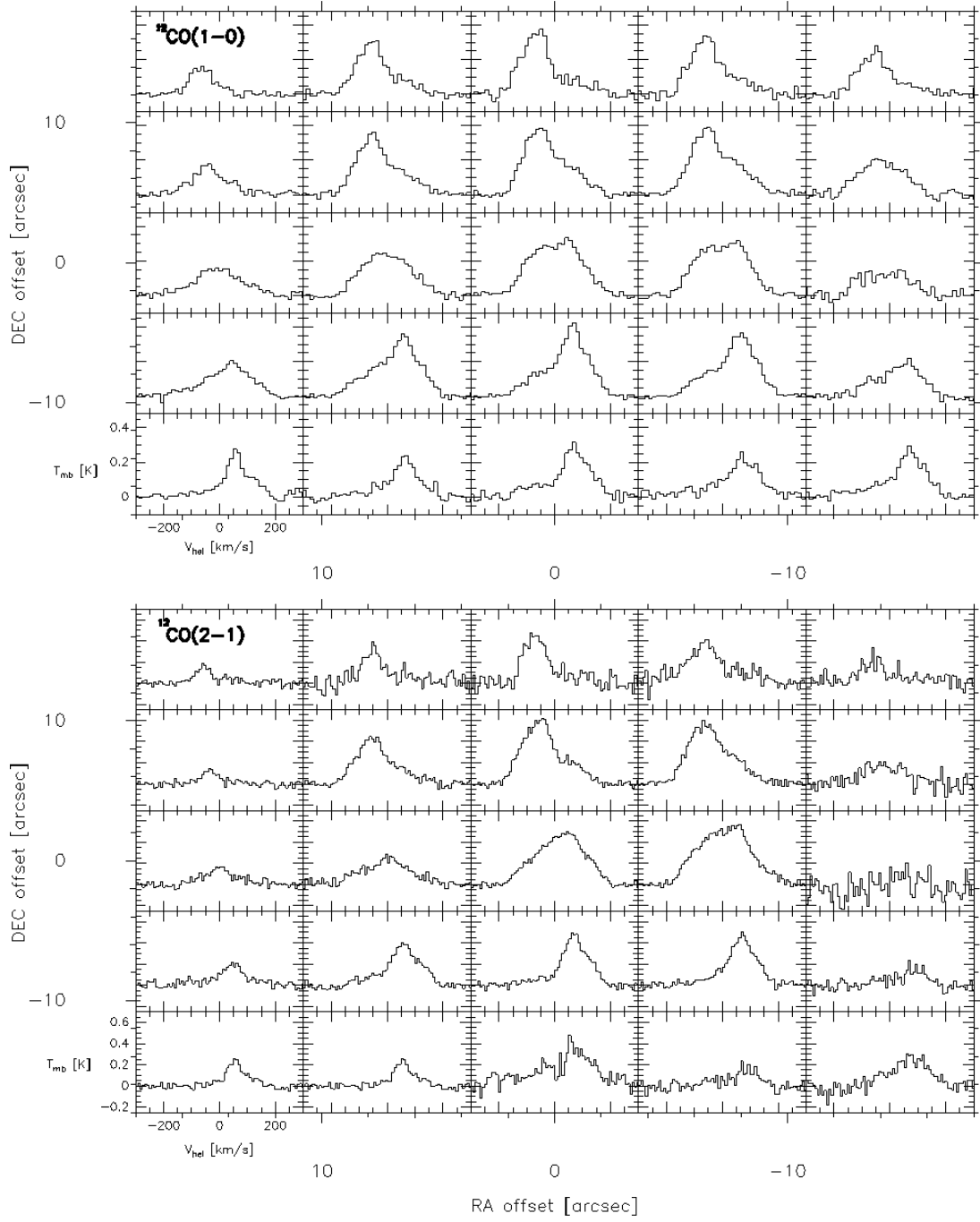


Fig. 1. Spectra maps of NGC 3627 made with the IRAM 30 m with 7'' spacing in $^{12}\text{CO}(1-0)$ [top] and $^{12}\text{CO}(2-1)$ [bottom]. The positions are arcsec offsets relative to the phase tracking center of our interferometric observations (see Table 1). Each spectrum has a velocity scale from -300 to 300 km s^{-1} , and a beam-averaged radiation temperature scale (T_{mb}) from -0.10 to 0.48 K for $^{12}\text{CO}(1-0)$ and from -0.25 to 0.70 K for $^{12}\text{CO}(2-1)$.

this position (see Table 1) and are not corrected for primary beam attenuation.

2.2. Single-dish observations

We performed IRAM 30 m telescope observations of NGC 3627 on July 16-19, 2002, in a 5×5 raster pattern with 7'' spacing. By using 4 SIS receivers, we simultaneously observed the frequencies of the $^{12}\text{CO}(1-0)$ [115 GHz], the

$^{12}\text{CO}(2-1)$ [230 GHz], and the $\text{HCN}(1-0)$ [89 GHz] lines. The $^{12}\text{CO}(2-1)$ line has been observed in dual-polarization. The half power beam widths (HPBW) are $22''$, $12''$, and $29''$ for $^{12}\text{CO}(1-0)$, $^{12}\text{CO}(2-1)$, and $\text{HCN}(1-0)$ lines, respectively. Typical system temperatures were ~ 110 – 145 K at 115 GHz, ~ 320 – 750 K at 230 GHz, and ~ 110 – 145 K at 89 GHz. For the single-dish data reduction, the Continuum and Line Analysis Single-dish Software (CLASS²) was used. Throughout the paper we express the line intensity scale in units of the beam-averaged radiation temperature (T_{mb}). T_{mb} is related to the equivalent antenna temperature reported above the atmosphere (T_A^*) by $\eta = T_A^*/T_{\text{mb}}$, where η is the telescope main-beam efficiency. At 115 GHz $\eta = 0.79$, at 230 GHz $\eta = 0.54$, and at 89 GHz $\eta = 0.82$. All observations were performed in “wobbler-switching” mode, with a minimum phase time for spectral line observations of 2 s and a maximum beam throw of $240''$. The pointing accuracy was $\sim 3''$ rms. The single-dish maps presented in this paper are centered on the phase tracking center of our interferometric observations (see Table 1).

2.3. Short spacing correction

An interferometer is limited by the minimum spacing of its antennas. Because two antennas can not be placed closer than some minimum distance (D_{min}), signals on spatial scales larger than some size ($\propto \lambda/D_{\text{min}}$) will be attenuated. This effect, called the “missing flux” problem, is resolved by using single-dish observations to compute short spacings and complete the interferometric measurements.

By combining 30 m and PdBI data, we found the best compromise between good angular resolution and complete restoration of the missing extended flux by varying the relative weights of 30 m and PdBI observations. The combined PdBI+30 m maps have angular resolutions of $2''.1 \times 1''.3$ at PA = 23° for the $^{12}\text{CO}(1-0)$ and $0''.9 \times 0''.6$ at PA = 30° for the $^{12}\text{CO}(2-1)$. In the combined maps, the rms uncertainty σ in 5 km s^{-1} width velocity channels is $3.6 \text{ mJy beam}^{-1}$ and $6.5 \text{ mJy beam}^{-1}$ for the $^{12}\text{CO}(1-0)$ and $^{12}\text{CO}(2-1)$ lines, respectively. For these maps, the conversion factors between intensity and brightness temperature are $32 \text{ K (Jy beam}^{-1})^{-1}$ at 115 GHz and $41 \text{ K (Jy beam}^{-1})^{-1}$ at 230 GHz. All interferometric figures presented in this paper are realized with short-spacing-corrected data.

Within $22''$, the $^{12}\text{CO}(1-0)$ HPBW for the 30 m telescope, the map including only PdBI observations recovers a flux $S_{\text{CO}(1-0)} = 251 \text{ Jy km s}^{-1}$, 70% of the total flux measured with the merged PdBI+30 m map, $S_{\text{CO}(1-0)} = 359 \text{ Jy km s}^{-1}$. Table 2 reports both $^{12}\text{CO}(1-0)$ flux values determined with our observations (single-dish, interferometric, and combined PdBI+30 m) and those present in literature. In this table, Col. (1) indicates the reference, Cols. (2) and (3) are the telescope (single-dish or interferometer) and the diameter of the single-dish telescope respectively, Col. (4) is the primary beam of the instrument or the diameter used for the performed photometry, Col. (5) is the beam in interferometric measurements, and Col. (6) gives the measured flux. Table 2 shows that $^{12}\text{CO}(1-0)$

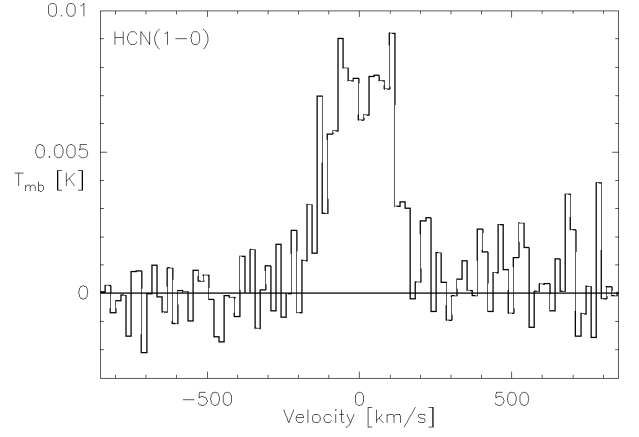


Fig. 2. $\text{HCN}(1-0)$ spectrum toward the center of NGC 3627, averaged over the 25-point map made with the IRAM 30 m with $7''$ spacing. The spectrum has a velocity scale from -850 to 850 km s^{-1} and a beam-averaged radiation temperature scale (T_{mb}) from -0.003 to 0.010 K .

fluxes we obtained with interferometric observations, single-dish, and combined measurements (PdBI+30 m) are in good mutual agreement with each other and with data present in literature. Our 30 m observations give a value $S_{\text{CO}(1-0)} = 343 \text{ Jy km s}^{-1}$ for the central position, consistent with flux value found with PdBI+30 m data within the $^{12}\text{CO}(1-0)$ 30 m-HPBW ($22''$). The whole region covered with 30 m observations ($\sim 50'' \times 50''$) gives a flux of $1097 \text{ Jy km s}^{-1}$, in agreement with the BIMA SONG survey³ (NRAO 12 m) measurements (Helfer et al. 2003, see Fig. 50, ~ 1100 – $1200 \text{ Jy km s}^{-1}$). Moreover, within the $42''$ primary beam field of the PdBI, we recovered $\sim 85\%$ of the flux detected by Young et al. (1995) for the central position with the FCRAO (786 Jy km s^{-1}), a good agreement considering the uncertainties in the amplitude calibration and the non-correction by the primary beam attenuation.

2.4. Other images of NGC 3627

We also acquired the large-scale $^{12}\text{CO}(1-0)$ emission image available thanks to the BIMA SONG survey performed with the 10-element BIMA millimeter interferometer (Welch et al. 1996) at Hat Creek, California. This image was first published by Regan et al. (2001) and Helfer et al. (2003), and covers a field of $350'' \times 410''$ (centered on the galaxy) with a pixel size of $1''$, and a beam of $6''.6 \times 5''.5$.

Several infrared (IR) images are included in our analysis: the *Spitzer*-IRAC $3.6 \mu\text{m}$ image (to trace the stellar component), the *Spitzer*-IRAC $8 \mu\text{m}$ image (to visualize the Polycyclic Aromatic Hydrocarbons [PAH] features), and the *Spitzer*-MIPS 70 and $160 \mu\text{m}$ images (to study the dust emission and resolve the SF regions). These IR images are avail-

³ Berkley-Illinois-Maryland Association Survey of Nearby Galaxies.

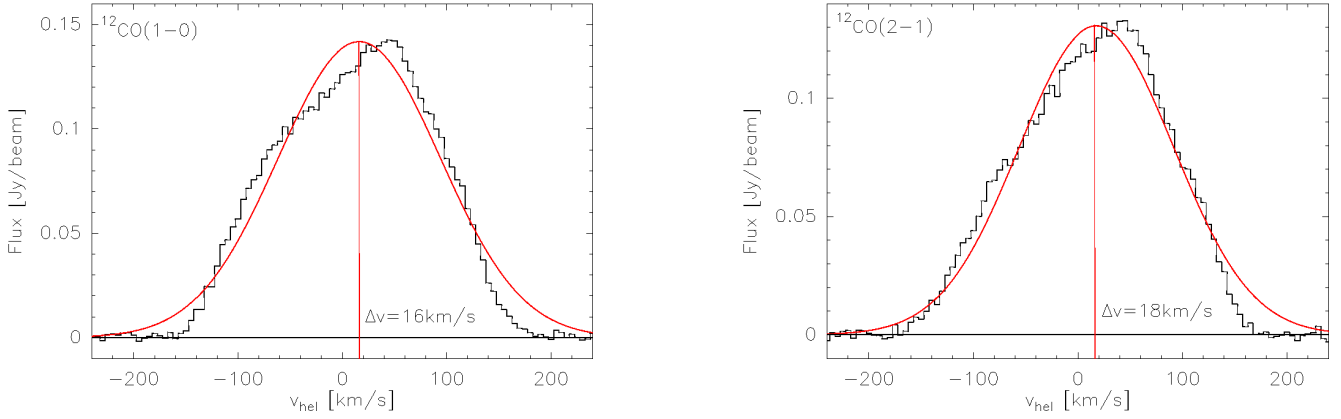


Fig. 3. *Left panel:* $^{12}\text{CO}(1-0)$ integrated spectrum and gaussian fit (red) in the inner $\sim 2''$ of NGC 3627 for PdBI+30 m combined data. The gaussian fit shows that the heliocentric systematic velocity is redshifted by 16 km s^{-1} with respect to the heliocentric velocity of the center (0 km s^{-1}). *Right panel:* Same for $^{12}\text{CO}(2-1)$. The gaussian fit shows that the heliocentric systematic velocity is redshifted by 18 km s^{-1} .

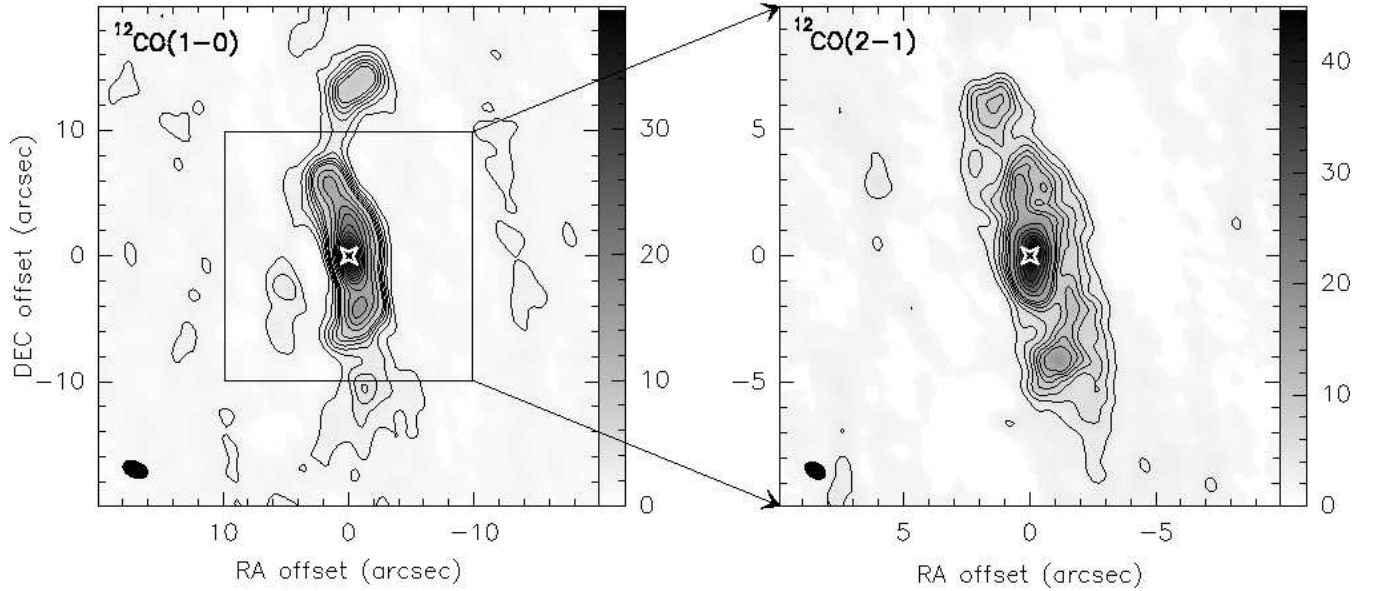


Fig. 4. *Left panel:* $^{12}\text{CO}(1-0)$ integrated intensity contours observed with the IRAM PdBI+30 m toward the center of NGC 3627. The white star marks the coordinates of the dynamical center of the galaxy coincident with our phase tracking center (see Table 1), with offsets in arcseconds. The map, derived with 2σ clipping, has not been corrected for primary beam attenuation. The *rms* noise level is $\sigma = 0.16 \text{ Jy beam}^{-1} \text{ km s}^{-1}$ and contour levels run from 3σ to 33σ with 6σ spacing and from 39σ to the maximum with 18σ spacing. In this map the $\pm 200 \text{ km s}^{-1}$ velocity range is used. The beam of $2''.1 \times 1''.3$ is plotted in the lower left. *Right panel:* Same for $^{12}\text{CO}(2-1)$. The *rms* noise level is $\sigma = 0.30 \text{ Jy beam}^{-1} \text{ km s}^{-1}$ and contour levels run from 3σ to 39σ with 6σ spacing and from 45σ to the maximum with 18σ spacing. The beam of $0''.9 \times 0''.6$ is plotted at lower left.

able thanks to the project “SINGS: The Spitzer Infrared Nearby Galaxies Survey” (Kennicutt et al. 2003). The IRAC images cover a sky area of $\sim 1600'' \times 1890''$ and $\sim 1220'' \times 1420''$ at $3.6 \mu\text{m}$ and $8 \mu\text{m}$ respectively, both with a pixel size of $0''.75$, and spatial resolutions of $\sim 1-2''$. The MIPS $70 \mu\text{m}$ image covers $\sim 1940'' \times 3645''$ with a pixel size of $4''.5$, and the MIPS $160 \mu\text{m}$ image $\sim 2025'' \times 3460''$ with a pixel size of $9''$.

We also use two near-infrared (NIR) images H ($1.65 \mu\text{m}$): the first was taken from the Two Micron All Sky Survey (2MASS) and covers a FOV of $\sim 12' \times 12'$, with a resolution of $2''.5$. The second $1.6 \mu\text{m}$ H -band image of NGC 3627 is available thanks to the F160W filter on the Near-Infrared Camera and Multi-Object Spectrometer (NICMOS, camera 3 [NIC3]) on board the Hubble Space Telescope (*HST*). This image cov-

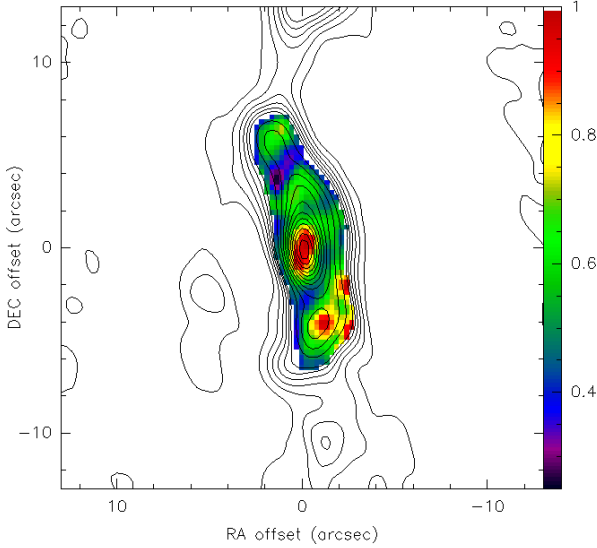


Fig. 5. Color scale of the CO(2–1)/CO(1–0) ratio map and $^{12}\text{CO}(1-0)$ intensity map contours as in Fig. 4 (left panel).

ers a FOV of $51'' \times 51''$, has a resolution of $0''.2$, and is not exactly centered on the galaxy but offset from our phase tracking center $7''$ toward west and $7''.4$ toward south. It is part of a survey of 94 nearby galaxies from the Revised Shapley Ames Catalog (Böker et al. 1999).

Finally, we also use a far-ultraviolet (FUV) image from the *GALEX* satellite, whose band is centered at $\lambda_{\text{eff}} = 1516 \text{ \AA}$. This image has been already used and studied in the context of the *GALEX* Nearby Galaxies Survey (NGS, Gil de Paz et al. 2007). The image covers a square region on the sky of size $\sim 5760'' \times 5760''$, i.e., much larger than the extent of the optical disk of NGC 3627, with $1''.5$ pixels. As the image was reduced with the *GALEX* data pipeline, it is already expressed in intensity units and skysubtracted. The total FUV calibrated magnitude is 16.34 ± 0.02 , corresponding to a FUV flux density of $1057 \pm 19 \mu\text{Jy}$.

3. Single-dish results

The observations performed with the A and B receivers of the IRAM 30 m telescope in the two ^{12}CO lines covered the inner $\sim 50''$, corresponding to the central $\sim 2.5 \text{ kpc}$ (in diameter) of the galaxy (Fig. 1). The observed positions show that the central region of NGC 3627 hosts extended molecular emission both in $^{12}\text{CO}(1-0)$ and $^{12}\text{CO}(2-1)$. The maximum detected T_{mb} is 0.4 K in $^{12}\text{CO}(1-0)$ at the offset position $(0'', -7'')$, and 0.6 K in $^{12}\text{CO}(2-1)$ at the offset position $(0'', 7'')$.

We estimate a flux of $1097 \text{ Jy km s}^{-1}$ within the inner $\sim 50'' \times 50''$ (see Table 2 and Sect. 2.3), in good agreement with previous single-dish flux determinations (e.g., Helfer et al. 2003). Assuming a H_2 -CO conversion factor of $X = N(\text{H}_2)/I_{\text{CO}} = 2.2 \times 10^{20} \text{ cm}^{-2} (\text{K km s}^{-1})^{-1}$ (Solomon & Barrett 1991), the $^{12}\text{CO}(1-0)$ integrated flux al-

lows us to derive the H_2 mass within the observed region as:

$$M_{\text{H}_2} [M_{\odot}] = 8.653 \times 10^3 D^2 [\text{Mpc}] S_{\text{CO}(1-0)} [\text{Jy km s}^{-1}] \quad (1)$$

We derive an H_2 mass of $M_{\text{H}_2} \sim 9.9 \times 10^8 M_{\odot}$ within the inner $\sim 50'' \times 50''$, and taking into account the mass of helium, the total molecular mass is $M_{\text{mol}} = M_{\text{H}_2 + \text{He}} = 1.36 \times M_{\text{H}_2} \sim 1.3 \times 10^9 M_{\odot}$.

The HCN(1–0) line has been observed for inner 25 positions with $7''$ spacing, covering the central $\sim 56''$ ($\sim 2.7 \text{ kpc}$ in diameter). The HCN(1–0) average spectrum over the 5×5 grid is displayed in Fig. 2 and shows a peak at $T_{\text{mb}} \sim 0.009 \text{ K}$. The HCN(1–0) velocity integrated intensity of the central position $(0'', 0'')$ is $I_{\text{HCN}(1-0)} = 3.1 \pm 0.3 \text{ K km s}^{-1}$ with $\Delta v = 237 \pm 32 \text{ km s}^{-1}$, consistent with the results obtained by Krips et al. (2008) for the same position observed with the same instrument ($I_{\text{HCN}(1-0)} = 2.7 \pm 0.2 \text{ K km s}^{-1}$ with $\Delta v = 290 \pm 30 \text{ km s}^{-1}$). The CO(1–0)/HCN(1–0) ratio averaged on the center of galaxy is roughly 10, a value intermediate between the ratios found in spatially resolved molecular disks around AGN, such as NGC 6951 (Krips et al. 2007) and NGC 1068 (Krips et al. 2008), and those found in pure starburst galaxies such as M 82 (Krips et al. 2008).

4. Interferometric results

4.1. Dynamical center

The phase tracking center of our observations (see Table 1) coincides almost exactly with the nuclear radio source detected at 15 GHz (VLA/2 cm) by Nagar et al. (2000) [$11^{\text{h}}20^{\text{m}}15.01^{\text{s}}$, $12^{\circ}59'29''.76$] and at 8.4 GHz (VLA/3.6 cm) by Filho et al. (2000) [$11^{\text{h}}20^{\text{m}}15.0^{\text{s}}$, $12^{\circ}59'30''$]. Thus, in the following, we assume that our observations are centered on the dynamical center of NGC 3627.

The spectral correlators were centered at 114.992 GHz for $^{12}\text{CO}(1-0)$ and 229.979 GHz for $^{12}\text{CO}(2-1)$, corresponding to $V_{\text{LSR}} = 727 \text{ km s}^{-1}$. Since for NGC 3627 the difference between LSR and heliocentric velocity is $\sim 0 \text{ km s}^{-1}$, our observations were centered on $V_{\text{LSR}} = V_{\text{hel}}(\text{PdBI}) = 727 \text{ km s}^{-1}$. In the inner $\sim 2''$ of NGC 3627 the velocity centroid is 16 km s^{-1} redshifted with respect to the heliocentric velocity of the center of our $^{12}\text{CO}(1-0)$ observations (Fig. 3, left panel). Similarly to $^{12}\text{CO}(1-0)$, for $^{12}\text{CO}(2-1)$ we find that the velocity centroid is 18 km s^{-1} redshifted with respect to the heliocentric velocity (Fig. 3, right panel). Assuming an intermediate value between the systemic heliocentric velocity determined for the $^{12}\text{CO}(1-0)$ and that for the $^{12}\text{CO}(2-1)$, we estimate $V_{\text{sys, hel}} = 744 \text{ km s}^{-1}$.

This estimation of the systemic heliocentric velocity is 24 km s^{-1} redshifted with respect to the systemic heliocentric velocity determined from H I observations (720 km s^{-1} , HyperLeda Database; Haan et al. 2008). In interacting galaxies and in those with a lopsided H I morphology, a discrepancy between systemic velocity derived from ^{12}CO and H I observations is not unusual. NGC 4579 (García-Burillo et al. 2009) and NGC 5953 (Casasola et al. 2010) exhibit differences of $\sim 50 \text{ km s}^{-1}$ between ^{12}CO and H I velocities, perhaps due to the interaction history of the galaxy and the different effect of the ram

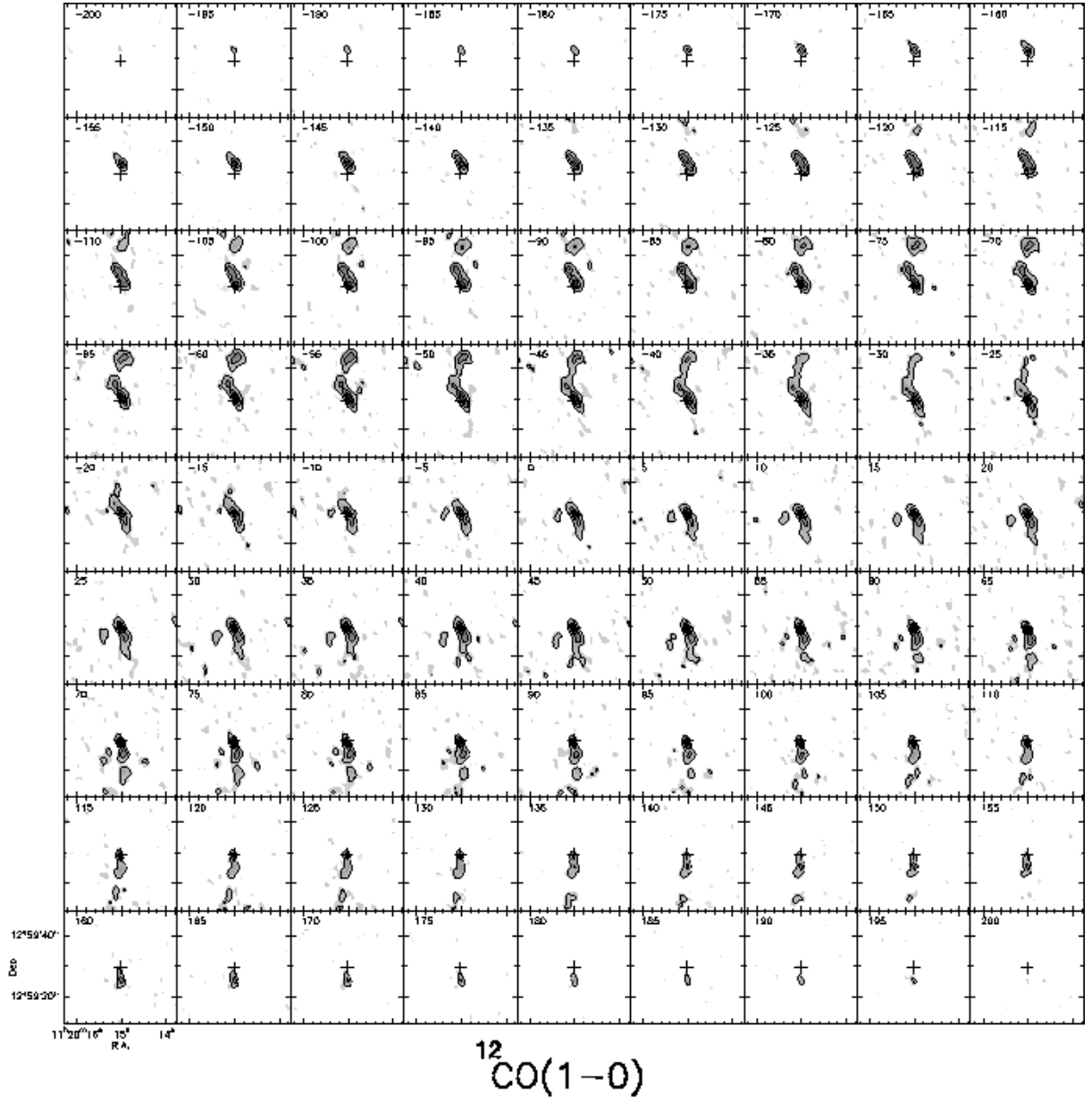


Fig. 6. $^{12}\text{CO}(1-0)$ velocity channel maps observed with the IRAM PdBI+30 m in the nucleus of NGC 3627, with a spatial resolution of $2''.1 \times 1''.3$ (HPBW). The maps are centered on the phase tracking center of our observations ($\alpha_{J2000} = 11^{\text{h}}20^{\text{m}}15.02^{\text{s}}$, $\delta_{J2000} = 12^{\circ}59'29''.50$) assumed to be coincident with the dynamical center of the galaxy. Velocity channels range from $\Delta V = -200 \text{ km s}^{-1}$ to $+200 \text{ km s}^{-1}$ in steps of 5 km s^{-1} relative to $V_{\text{sys, hel}} = 744 \text{ km s}^{-1}$ (see Sect. 4.1). The contours run from $-40 \text{ mJy beam}^{-1}$ to $260 \text{ mJy beam}^{-1}$ with spacings of 60 mJy beam^{-1} .

pressure on the atomic and molecular gas (García-Burillo et al. 2009). In NGC 3627, the role of interaction history and the ram-pressure, although not negligible, could have shifted the H I barycenter with respect to the molecular one less strongly than in NGC 4579 and NGC 5953.

4.2. CO distribution and mass

Figure 4 shows the $^{12}\text{CO}(1-0)$ and $^{12}\text{CO}(2-1)$ integrated intensity distributions in the inner $\sim 40''$ ($\sim 2 \text{ kpc}$) of NGC 3627. The $^{12}\text{CO}(1-0)$ emission (Fig. 4, left panel) exhibits a peak at the nucleus, extends along a bar-like structure of $\sim 18''$ ($\sim 900 \text{ pc}$) diameter with a north/south orientation (see later Sect. 4.4 for the discussion on the PA) and two peaks at its extremes, at $r \sim 5-6''$ ($\sim 270 \text{ pc}$), with the southern one more evident. The

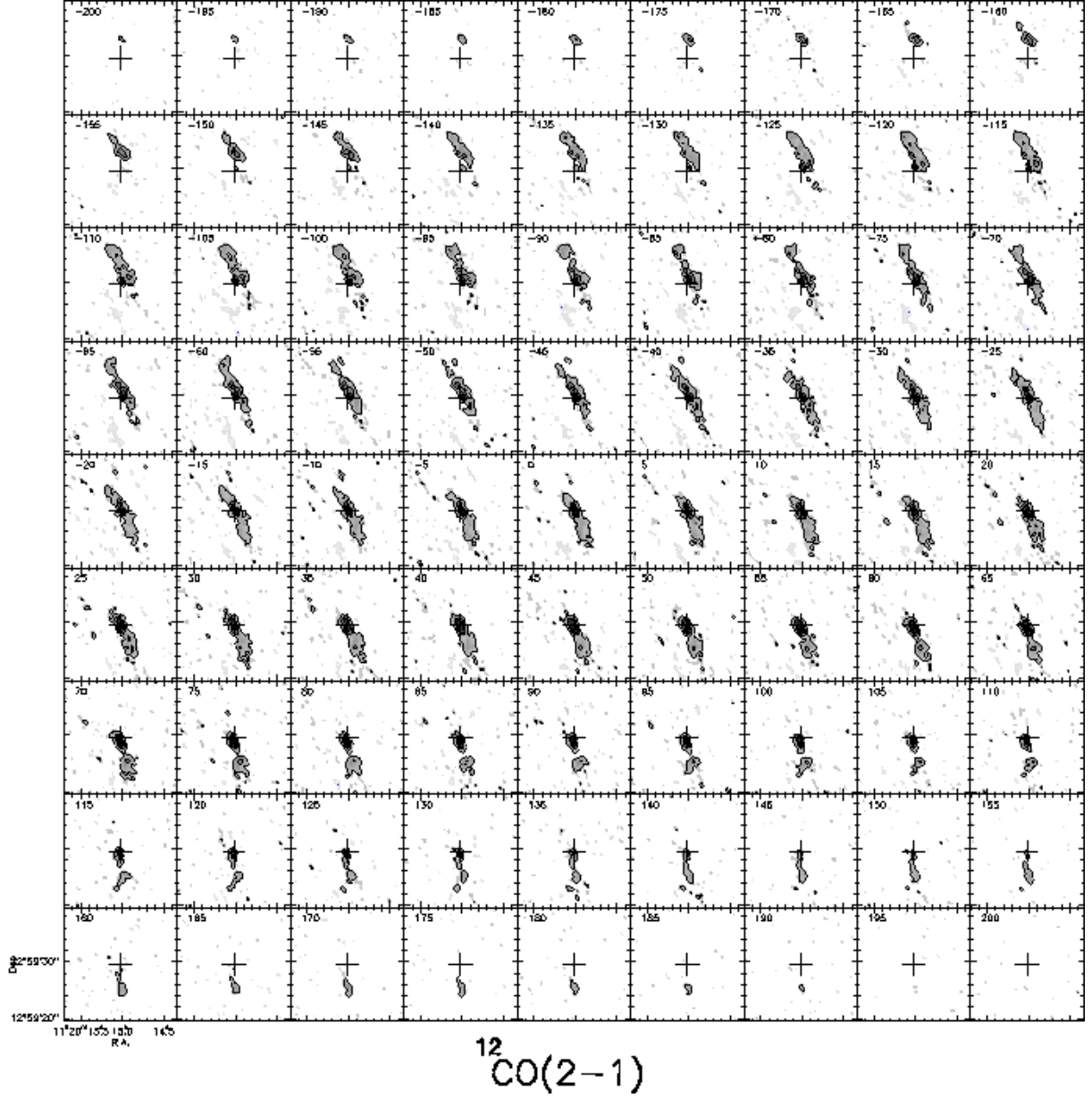


Fig. 7. Same as Fig. 6 but for the $^{12}\text{CO}(2-1)$ line, with a spatial resolution of $0''.9 \times 0''.6$. The contours run from $-50 \text{ mJy beam}^{-1}$ to $350 \text{ mJy beam}^{-1}$ with spacings of 50 mJy beam^{-1} .

$^{12}\text{CO}(1-0)$ morphology also shows a two-arm spiral feature from $r \sim 9''$ ($\sim 450 \text{ pc}$) to $r \sim 16''$ ($\sim 800 \text{ pc}$), with two peaks over these spiral arms at $r \sim 12-14''$ ($\sim 650 \text{ pc}$). A similar and more resolved distribution is found in $^{12}\text{CO}(2-1)$ [Fig. 4, right panel]. Like the nuclear peak, the two peaks at the ends of the inner $\sim 18''$ bar-like structure at $r \sim 5-6''$, are more evident than in $^{12}\text{CO}(1-0)$.

The ^{12}CO distribution found here agrees well with previous molecular gas maps, such as that given by Regan et al. (2001) and Helfer et al. (2003) in the context of the BIMA SONG survey and that obtained by Kuno et al. (2007) with the 45 m telescope of the Nobeyama Radio Observatory. Although we only

observed the inner $\sim 2 \text{ kpc}$ of the galaxy, the good PdBI resolution allows us to investigate the nuclear molecular gas distribution in NGC 3627 more in detail than in BIMA SONG survey (typical resolution of $\sim 6''$) and with the 45 m NRAO telescope (FWHM $\sim 15''$). The ^{12}CO distribution is completely different from the ringed H I morphology which exhibits an inner hole where instead the molecular gas is located (Haan et al. 2008; Walter et al. 2008).

Applying Eq. (1) to combined PdBI+30 m data, we derived a total H_2 mass of $M_{\text{H}_2} \sim 6.0 \times 10^8 M_{\odot}$ ($S_{\text{CO}} = 668 \text{ Jy km s}^{-1}$, see Table 2) within the $42''$ primary beam field of the PdBI. Taking into account the mass of helium, the total molecular mass is

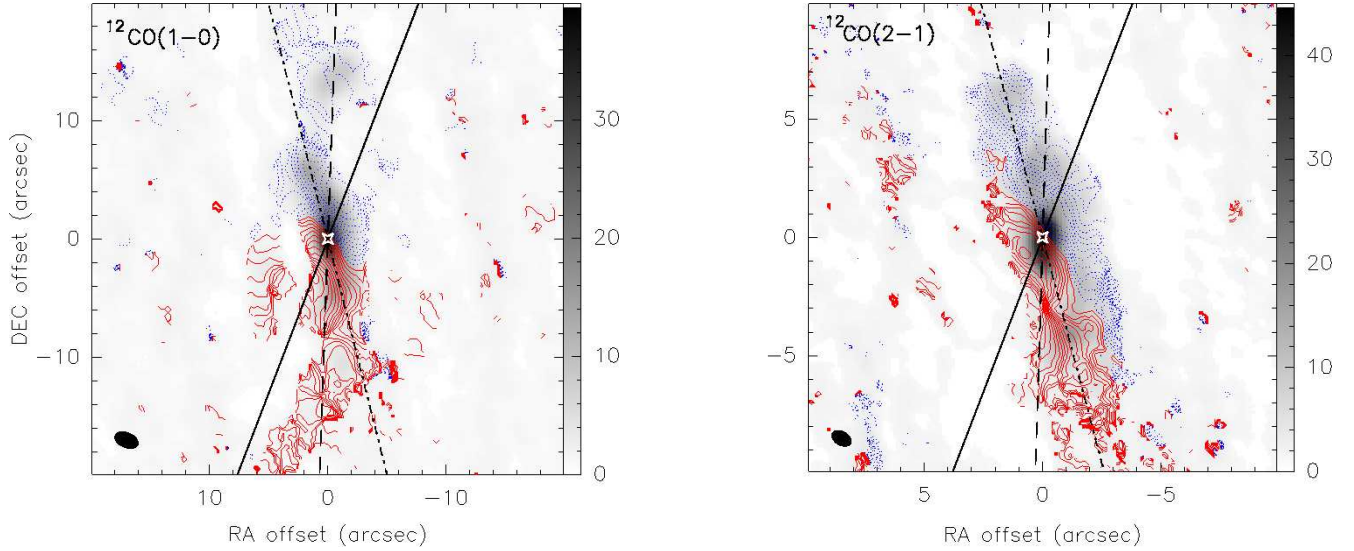


Fig. 8. *Left panel:* Overlay of the integrated $^{12}\text{CO}(1-0)$ emission, same as Fig. 4 (left panel), with CO mean-velocity field in contours spanning the range -180 to 180 km s^{-1} in steps of 10 km s^{-1} . The white star indicates the dynamical center of the galaxy. The velocities are referred to $V_{\text{sys, hel}} = 744 \text{ km s}^{-1}$, solid (red) lines are used for positive velocities, and dashed (blue) lines for negative velocities. The dashed line indicates the position angle of the major axis of the whole observed region ($\text{PA} = 178^\circ \pm 1^\circ$), while the dot-dashed line traces the position angle of the major axis of the bar-like structure ($\text{PA} = 14^\circ \pm 2^\circ$). The continuum line indicates the position angle of the primary stellar bar identified with the NIR H -band 2MASS image ($\text{PA} = -21^\circ$) [see later the left panel of Fig. 16 and Sect. 5.2]. *Right panel:* Same for $^{12}\text{CO}(2-1)$. The dashed line indicates the position angle of the major axis of the whole $^{12}\text{CO}(1-0)$ observed region ($\text{PA} = 178^\circ \pm 1^\circ$, see left panel), while the dot-dashed line traces the position angle of the major axis of the $^{12}\text{CO}(2-1)$ bar-like structure ($\text{PA} = 15^\circ \pm 2^\circ$). The continuum line indicates the position angle of the primary stellar bar identified with the NIR H -band 2MASS image ($\text{PA} = -21^\circ$) [see later Fig. 16 and Sect. 5.2].

$M_{\text{mol}} \sim 8.2 \times 10^8 M_\odot$. This is roughly 63% of the molecular gas mass within a $50''$ diameter (see Sect. 3). The $\sim 18''$ $^{12}\text{CO}(1-0)$ bar-like structure contributes an H_2 mass of $M_{\text{H}_2} \sim 2.1 \times 10^8 M_\odot$, roughly one-third of the H_2 mass computed within $42''$, although the feature occupies an area of only $\sim 5\%$ of the $42''$ beam. NGC 3627, compared to other NUGA galaxies, is not particularly massive in molecular gas, especially with respect to the extraordinary case of NGC 1961 with an H_2 mass of $\sim 1.8 \times 10^{10} M_\odot$ (Combes et al. 2009).

4.3. $\text{CO}(2-1)/\text{CO}(1-0)$ line ratio

Information about the local excitation conditions of the molecular gas can be inferred from the line ratio $R_{21} = I_{21}/I_{10}$. This ratio is obtained by comparing the ^{12}CO maps of the two transitions, at the same resolution and with the same spatial frequency sampling. Figure 5 shows R_{21} ratio with $^{12}\text{CO}(1-0)$ contours as in Fig. 4 (left panel). In the observed region, the line ratio ranges from 0.25 to 1 but the bulk of the emission has a ratio between 0.4 and 0.7. These R_{21} line ratio values are consistent with $R_{21} = 0.6$ obtained by Krips et al. (2008), and more in general with optically thick emission in spiral disks (e.g., Braine & Combes 1992; García-Burillo et al. 1993). The R_{21} peaks of ~ 1 are reached in the center of NGC 3627 and at the southern extreme of the elongated ^{12}CO emission region.

A higher excitation of the molecular gas in the nucleus, suggested by a higher R_{21} line ratio, is consistent with the $\text{HCN}(1-0)$ emission in the same region (see Sect. 3).

4.4. CO Kinematics

Figures 6 and 7 show the velocity-channel maps of $^{12}\text{CO}(1-0)$ and $^{12}\text{CO}(2-1)$ emission, respectively, in the central region of NGC 3627. The inner ^{12}CO emission of the galaxy exhibits signatures of non-circular motions both at negative and positive velocities. These non-circular components are associated both with the $18''$ bar-like structure and the spiral feature detected beyond the bar-like structure and will be discussed in detail later, in Sect. 4.5, where we analyze the rotation curve derived with our ^{12}CO data.

$^{12}\text{CO}(1-0)$ isovelocity contours (first-moment map) are superposed on the $^{12}\text{CO}(1-0)$ integrated intensity in Figure 8 (left panel). The white star indicates the dynamical center of the galaxy, assumed coincident with the phase tracking center of our observations, and the velocities are relative to the systemic heliocentric velocity, $V_{\text{sys, hel}} = 744 \text{ km s}^{-1}$ (see Sect. 4.1). The dashed line traces the position angle of the major axis of the observed region, $\text{PA} = 178^\circ \pm 1^\circ$ (almost vertical), obtained by maximizing the symmetry in the position velocity diagrams. This position angle is close to that of the entire galaxy, as given

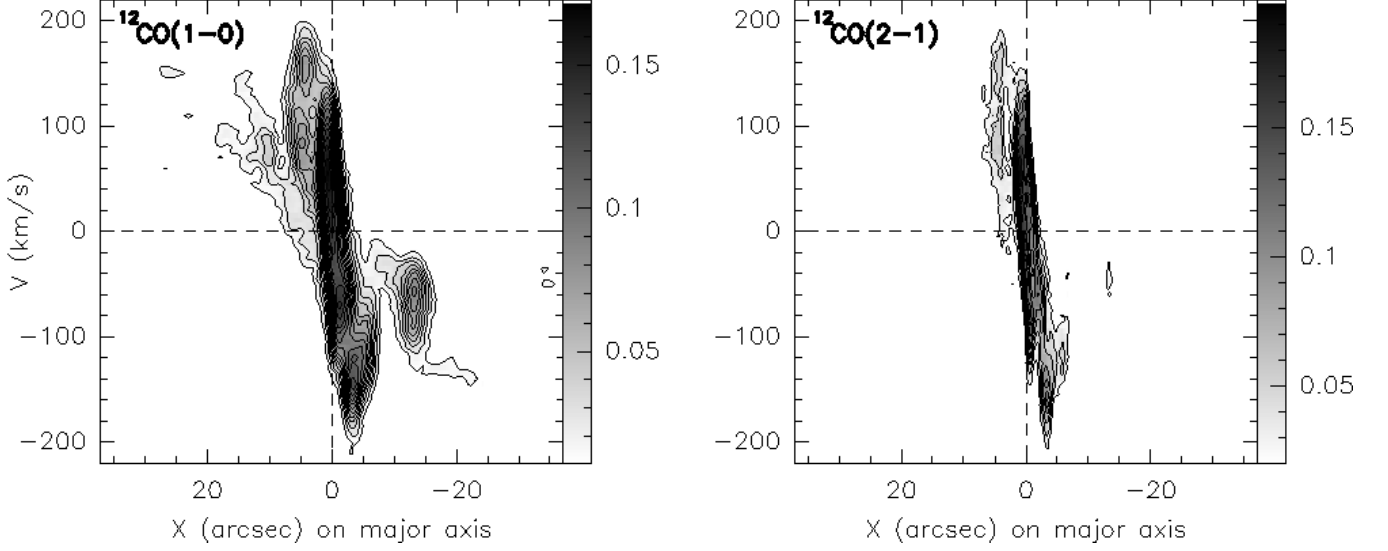


Fig. 9. *Left panel:* $^{12}\text{CO}(1-0)$ position-velocity diagram along the major axis ($\text{PA} = 178^\circ$) of NGC 3627 using the velocity range from -220 to 220 km s^{-1} contoured over a grey-scale representation. Contour levels are from 3σ to 48σ in steps of 3σ ($\sigma=3.6 \text{ mJy beam}^{-1}$). The velocities are relative to $V_{\text{sys, hel}} (= 744 \text{ km s}^{-1})$ and X are the offsets along the major axis in arcsecs. *Right panel:* The same for $^{12}\text{CO}(2-1)$. Contour levels are from 3σ to 30σ in steps of 3σ ($\sigma=6.7 \text{ mJy beam}^{-1}$).

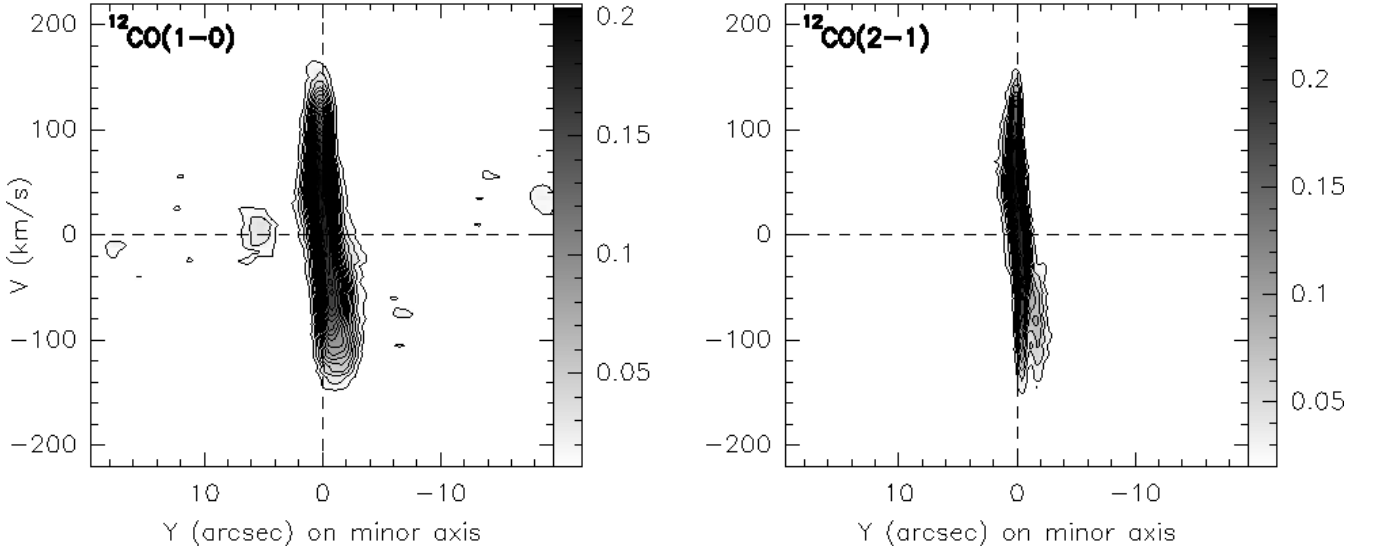


Fig. 10. *Left panel:* Same as Fig. 9 along the minor axis ($\text{PA} = 88^\circ$) of NGC 3627. Contour levels are from 3σ to 57σ in steps of 3σ ($\sigma=3.6 \text{ mJy beam}^{-1}$). Y are the offsets along the minor axis in arcsecs. *Right panel:* The same for $^{12}\text{CO}(2-1)$. Contour levels are from 3σ to 35σ in steps of 3σ ($\sigma=6.7 \text{ mJy beam}^{-1}$).

by the surface brightness profiles (172° , see Sect. 5.2), and given in the Uppsala General Catalog (173°). The dot-dashed line traces the position angle of the major axis of the bar-like structure, $\text{PA} = 14^\circ \pm 2^\circ$. The right panel of Fig. 8 shows $^{12}\text{CO}(2-1)$ isovelocity contours on the $^{12}\text{CO}(2-1)$ integrated intensity, where the position angle of the major axis of the observed region is very similar to that found for the $^{12}\text{CO}(1-0)$ inner region ($\text{PA} = 15^\circ \pm 2^\circ$). The continuous lines, in the left

and right panels of Fig. 8, show the PA of the stellar bar identified in the NIR with the H -band 2MASS image ($\text{PA} = -21^\circ$) [see below the left panel of Fig. 16 and Sect. 5.2]. The different PAs of the stellar bar and the molecular gas bar-like structure suggest that the gas is leading the stellar bar. Signatures of non-circular motions are visible also in Fig. 8, since the isovelocity contours appear severely tilted along the molecular gas bar-like structure both in $^{12}\text{CO}(1-0)$ and $^{12}\text{CO}(2-1)$.

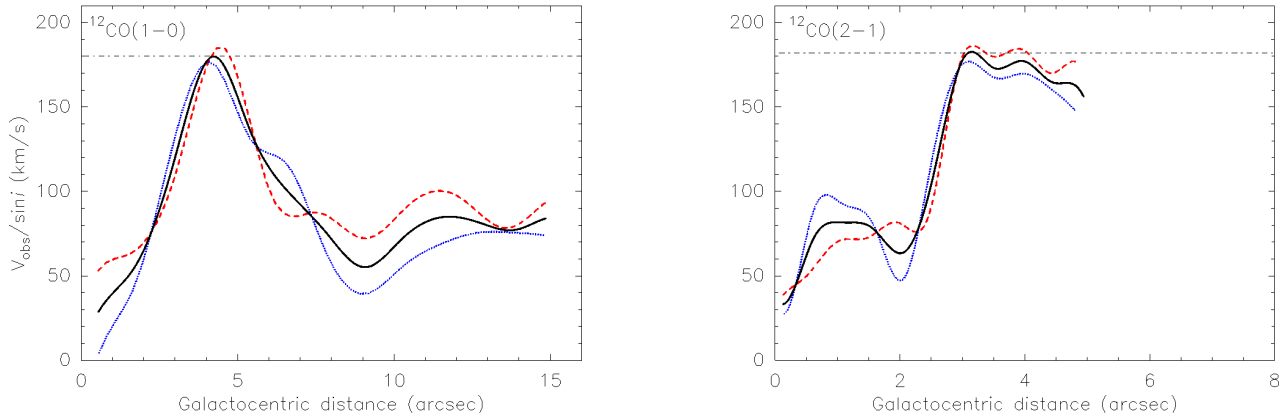


Fig. 11. *Left panel:* The $^{12}\text{CO}(1-0)$ RC derived as described in the text. The positive (negative) velocities, corrected for inclination, are shown as a red dashed (blue dotted) line; the black line shows the average. The horizontal dot-dashed line at 180 km s^{-1} indicates the velocity of the bulk of the molecular gas. *Right panel:* The same as the left panel, but for $^{12}\text{CO}(2-1)$.

Figures 9 and 10 show position-velocity (p-v) cuts along the major (PA = 178°) and minor axis (PA = 88°) of NGC 3627, respectively. In both figures, the $^{12}\text{CO}(1-0)$ emission is given in the left panel and $^{12}\text{CO}(2-1)$ in the right. Our p-v plots along major axis are consistent with the $^{12}\text{CO}(1-0)$ p-v diagram obtained by Regan et al. (2002), where the different velocity range between nuclear region and bar ends is yet clearer, because they mapped in $^{12}\text{CO}(1-0)$ the whole galaxy. Regan et al. (2002)’s p-v diagram (Fig. 5a in their paper) shows that the components we found at $10\text{--}15''$ from the center at velocities of $60\text{--}80 \text{ km s}^{-1}$ (not corrected for inclination) maintain this velocity also at larger radii (until $\sim 50''$ from the center), and then again increase and reach the velocity assumed by bar ends.

4.5. CO rotation curve and dynamical mass

We have derived a rotation curve (RC) from the p-v diagram along the kinematic major axis of NGC 3627 (PA = 178°). By fitting multiple gaussian profiles to the spectra across the major axis we calculated the terminal velocities, and the fitted velocity centroids, corrected for inclination ($\sin i$, $i = 61.3^\circ$), give $V_{\text{obs}}/\sin i$ for each galactocentric distance. Figure 11 shows RCs for $^{12}\text{CO}(1-0)$ [left] $^{12}\text{CO}(2-1)$ [right], where for each line we plotted both the two curves derived from either side of the major axis and their combination into a average by spline interpolation. This interpolation is justified by the similar behavior of the positive velocity curve and the negative velocities for both lines.

The $^{12}\text{CO}(1-0)$ RC reaches a maximum of 180 km s^{-1} (velocity corrected for inclination) at $r \sim 4.3''$ ($\sim 0.2 \text{ kpc}$), and then decreases until velocities between $\sim 60 \text{ km s}^{-1}$ and $\sim 85 \text{ km s}^{-1}$ maintaining these velocities until $\sim 15''$ ($\sim 0.74 \text{ kpc}$) from the center (Fig. 11, left panel). The $^{12}\text{CO}(2-1)$ RC shows a similar maximum velocity, $\sim 183 \text{ km s}^{-1}$, reached at $r < 5''$ (Fig. 11, right panel). At larger distances from the nucleus ($r > 15''$), we expect that the RC again increases until $\sim 180 \text{ km s}^{-1}$, the velocity at the ends of the bar, consistently with p-v plots mapping the

whole galaxy (e.g., Regan et al. 2002). Asymmetries are also seen in the H α RC of NGC 3627 (Chemin et al. 2003), both in the inner disk (between $25''$ and $34''$ from the nucleus, already outside the range of our ^{12}CO observations) and at larger radii ($> 88''$). The form of the RC of NGC 3627, with remarkable dips in velocity near the nucleus, is not unusual for galaxies with circumnuclear bars or gas disks (e.g., Rubin et al. 1997).

Such behavior often reflects non-circular motions depending both on the internal structure of the galaxy (e.g., the bar and consequent streaming motions) and the orbital parameters of the interaction with nearby companions. Another important source of non-circular motions may be the kinematic feedback to the gas from star formation (Beauvais & Bothun 1999). Regions of intense SF and turbulent motions in those regions may lead to an increase in the local velocity dispersion. In NGC 3627, the dips may be due to all three mechanisms, a combination of the effects of the interaction, the strong bar, and the kinematic feedback to the gas from SF.

From the RC, we can estimate the dynamical mass within a certain radius with the formula $M(R) = 2.325 \times 10^5 \alpha R V^2(R)$ where $M(R)$ is in M_\odot , R in kpc, V in km s^{-1} , and α is a factor related to the geometry. The choice of V to use in the above formula is complicated by the presence of dips in the RC (Fig. 11). Although these dips are due to non-circular motions, at larger radii both CO (e.g., Regan et al. 2002) and H α (e.g., Zhang et al. 1993; Haan et al. 2008) RCs are flat and at the same velocity found at the bar ends. We can thus estimate the dynamical mass using the maximum velocity of 180 km s^{-1} (corrected for inclination) reached at $\sim 210 \text{ pc}$ from the center.

Assuming for α a value of 0.8, intermediate between the value appropriate for a spherical distribution (1.0) and that for a flat disk (0.6), the above formula gives a dynamical mass of $M_{\text{dyn}} = 1.3 \times 10^9 M_\odot$ within a radius of $4.3''$ ($\sim 0.2 \text{ kpc}$). Continuing to neglect non-circular motions and assuming a roughly flat RC also at larger radii, the dynamical mass should be $M_{\text{dyn}} = 6.0 \times 10^9 M_\odot$ within a radius of $21''$ ($\sim 1 \text{ kpc}$). In the same region, we estimate a H_2 mass of $\sim 6.0 \times 10^8 M_\odot$ (see

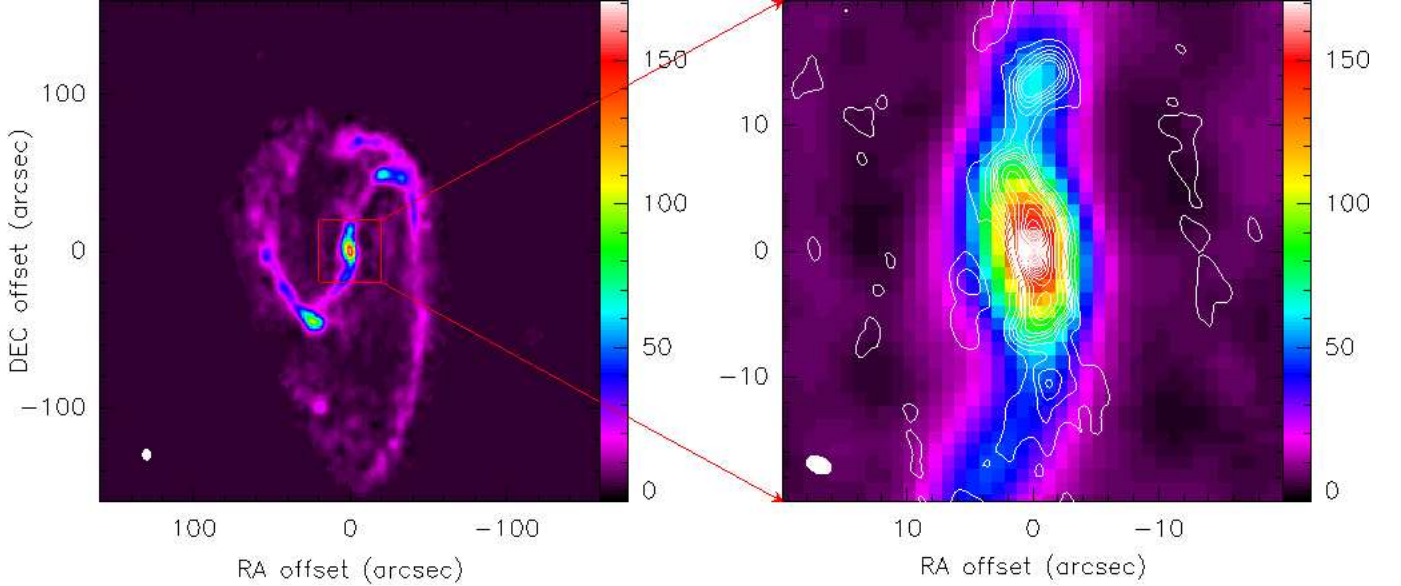


Fig. 12. *Left panel:* The BIMA SONG $^{12}\text{CO}(1-0)$ emission image of NGC 3627 (Regan et al. 2001). The beam of $6''.6 \times 5''.5$ is plotted in the lower left. The inner $320''$ are shown. *Right panel:* NUGA $^{12}\text{CO}(1-0)$ contours (in white) as in Fig. 4 (left panel) overlaid on the BIMA SONG $^{12}\text{CO}(1-0)$ emission image. The $^{12}\text{CO}(1-0)$ NUGA beam of $2''.1 \times 1''.3$ is plotted in the lower left. The inner $40''$ are shown.

Sect. 4.2), $\sim 10\%$ of the dynamical mass. Zhang et al. (1993) found a dynamical mass of $M_{\text{dyn}} = 5.8 \times 10^9 M_{\odot}$ (value scaled to our adopted distance of $D = 10.2 \text{ Mpc}$) within a radius of $23''$, a value consistent with our determination in a similar region, considering uncertainties from a different assumed inclination and rotation velocity. Moreover, Zhang et al. (1993) found a ratio $M_{\text{H}_2}/M_{\text{dyn}} \sim 11\%$ within the radius of $23''$, similar to our value. Nevertheless, because of the clear signature of non-circular motions in the RC, our estimate of dynamical mass is very uncertain, probably $\pm 50\%$.

5. Comparison with other data

Here we present a comparison of our ^{12}CO observations and images at other wavelengths available for NGC 3627. These comparisons allow both to assess possible correlations between different tracers of the ISM and to determine the location of the dynamical resonances, useful for probing gas inflow in the circumnuclear region of the galaxy. All images have been centered on the phase tracking center of our ^{12}CO interferometric observations (see Table 1), and -when necessary- properly rotated with North up and E left.

5.1. Another CO map: NUGA vs. BIMA SONG

The left panel of Figure 12 shows the BIMA SONG $^{12}\text{CO}(1-0)$ emission image of NGC 3627. This image reveals, like in the optical, a nuclear barred structure and a pronounced and asymmetric spiral pattern. A close-up of the inner $40''$ of the BIMA SONG $^{12}\text{CO}(1-0)$ map with our $^{12}\text{CO}(1-0)$ contours overlaid,

as in Fig. 4 (left panel), is shown in the right panel of Fig. 12. The two ^{12}CO data sets agree quite well; the only significant disagreement is present toward the south, where our higher-resolution $^{12}\text{CO}(1-0)$ contours delineate a barred structure that develops mainly toward the south, while the BIMA SONG $^{12}\text{CO}(1-0)$ emission is more rotated toward the east/south-east.

5.2. Near- and mid-infrared emission

NIR images of NGC 3627 have been used both to derive the surface brightness profiles and to perform comparisons with our ^{12}CO observations. We compared the surface brightness profiles of the ground- and space-based images by extracting elliptically averaged profiles, centered on the brightness peaks. The position angle and ellipticity were allowed to vary in the ellipse fitting. These radial profiles are shown in Figure 13, where the dashed horizontal lines in the lower panels correspond to the adopted position angle (PA) and inclination (i). The three profiles (*HST* F160W represented by the solid (blue) line, IRAC $3.6 \mu\text{m}$ by the dotted (green) line, and IRAC $8 \mu\text{m}$ by the dashed (red) line) are quite similar, in particular the *HST* F160W and the IRAC $3.6 \mu\text{m}$ profiles show a similar trend within the inner $10''$. Also shown are the runs of ellipticity ϵ , ellipse position angle θ , and $\cos(4\theta)$ residuals of the ellipse fitting. The adopted PA is 178° (see Sect. 4.4), similar to the fitted PA of 172° . The inclination computed from the elliptical fits of the IRAC $3.6 \mu\text{m}$ image converges to 61.3° , very close to the inclination given by NED, 62.5° .

Figure 14 shows a large-scale view of NGC 3627 at $8 \mu\text{m}$ (*Spitzer*-IRAC). The longest-wavelength $8 \mu\text{m}$ IRAC band is

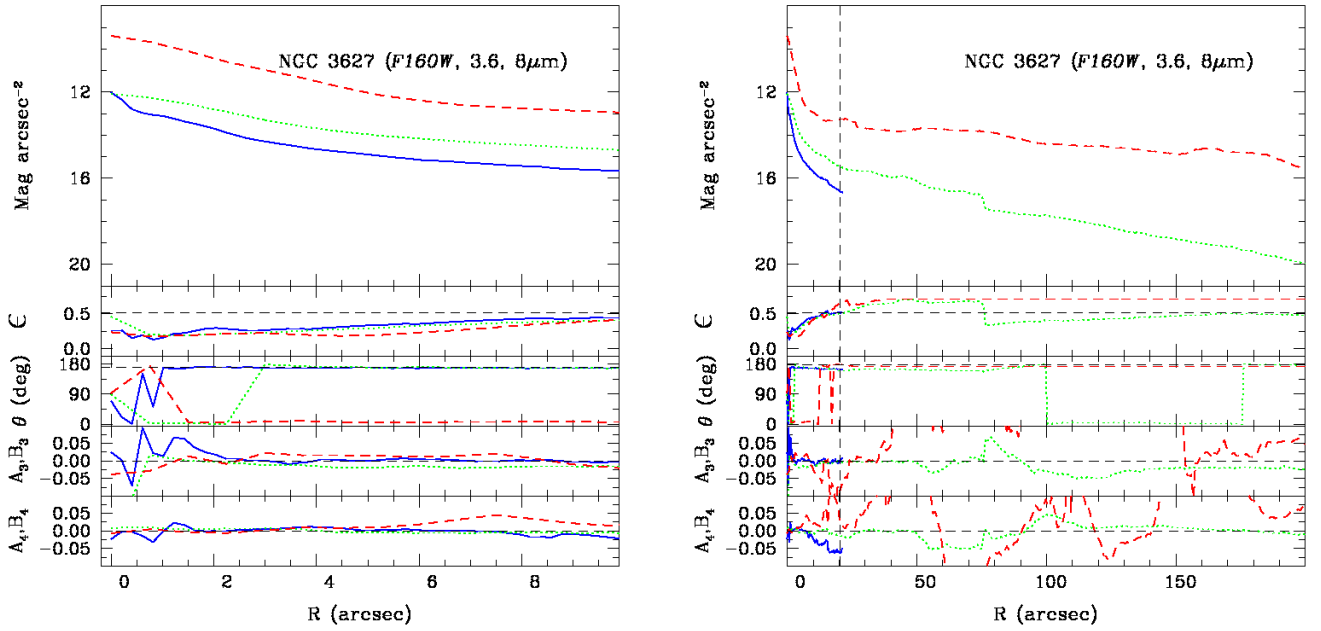


Fig. 13. The upper panels show radial surface brightness profiles of NGC 3627 made by fitting elliptical isophotes. The left panel shows a smaller FOV than the right panel. The solid (blue) line corresponds to *HST* F160W, the dotted (green) line to IRAC 3.6 μm , and the dashed (red) line to the IRAC 8 μm . The lower panels display the radial runs of ellipticity ϵ , position angle θ , and $\cos(4\theta)$ terms in the ellipse fitting residuals. The adopted PA (178° , see Sect. 4.4) and the best-fit inclination (61.3°) are shown by dashed horizontal lines in the lower panels. The dashed vertical line shows a radius of 1 kpc ($20''.4$).

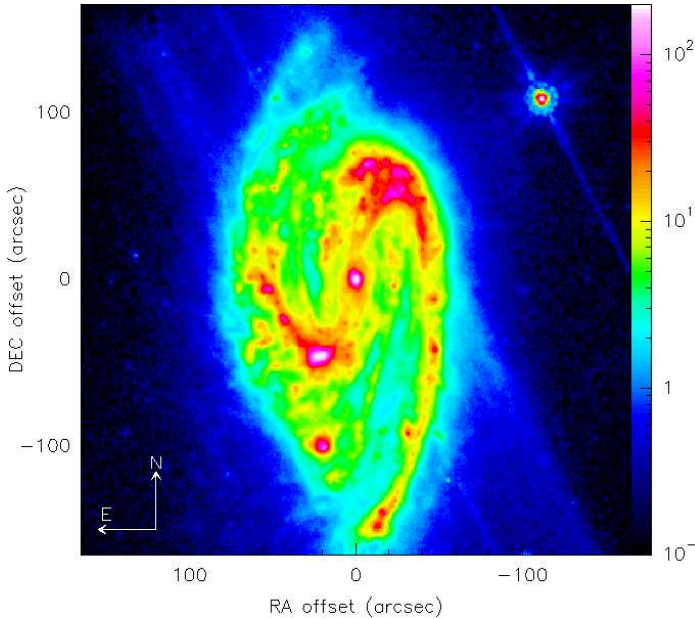


Fig. 14. The large-scale IRAC 8 μm image of NGC 3627 centered on the phase tracking center of our ^{12}CO interferometric observations. The inner $330''$ are shown.

emission. This figure clearly reveals a spiral pattern, asymmetric with respect to the major axis, and heavy dust lanes, signature of a strong density wave action. This image also shows an evident perturbed morphology of the eastern arm. The bulk of the inner warm dust emission appears configured in a smooth elongated (north/south) disk, but the large-scale bar seen in the BIMA-SONG CO image is clearly reflected in the 8 μm emission.

Figure 15 shows the stellar morphology traced by the 3.6 μm (*Spitzer*-IRAC) emission in the circumnuclear region of NGC 3627, with overlaid $^{12}\text{CO}(1-0)$ [left panel] and $^{12}\text{CO}(2-1)$ [right panel] intensity contours. This comparison shows that the large-scale 3.6 μm stellar bar and the molecular gas bar-like feature have different orientation in the plane of the galaxy. The stellar bar has a PA of -21° , while the molecular bar has a PA of $\sim 14^\circ$ in $^{12}\text{CO}(1-0)$ and $\sim 15^\circ$ in $^{12}\text{CO}(2-1)$ [see Sect. 4.4]. This difference in orientation suggests that the molecular gas is leading the stellar bar. The right panel of Fig. 13 shows clear signatures of a bar-like feature at 3.6 μm at a radius of $60-70''$: the surface brightness undergoes an inflection; the ellipticity dips; and the PA changes slightly. The bar would thus have a radius between 3 and 3.4 kpc.

The 1.6 μm (*H*-band, 2MASS) large-scale morphology of NGC 3627 is shown in the left panel of Figure 16. Most of the stellar mass in a typical galaxy is locked up in cool stars, whose light is emitted longward of 1 μm . Since the stellar spec-

dominated by PAHs and perhaps some hot dust continuum

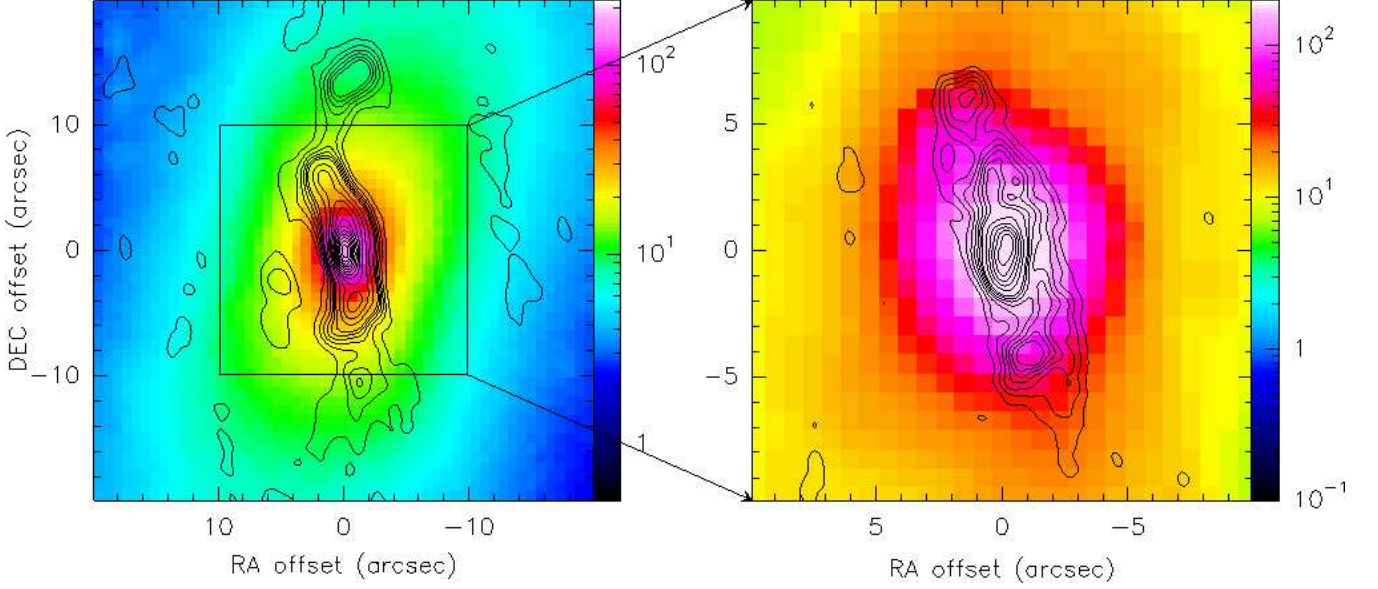


Fig. 15. *Left panel:* $^{12}\text{CO}(1-0)$ integrated intensity contours as in Fig. 4 (*left panel*) overlaid on the IRAC $3.6\mu\text{m}$ image of NGC 3627 in false color. The inner $40''$ are shown. *Right panel:* Same for $^{12}\text{CO}(2-1)$ integrated intensity contours as in Fig. 4 (*right panel*). The inner $20''$ are shown.

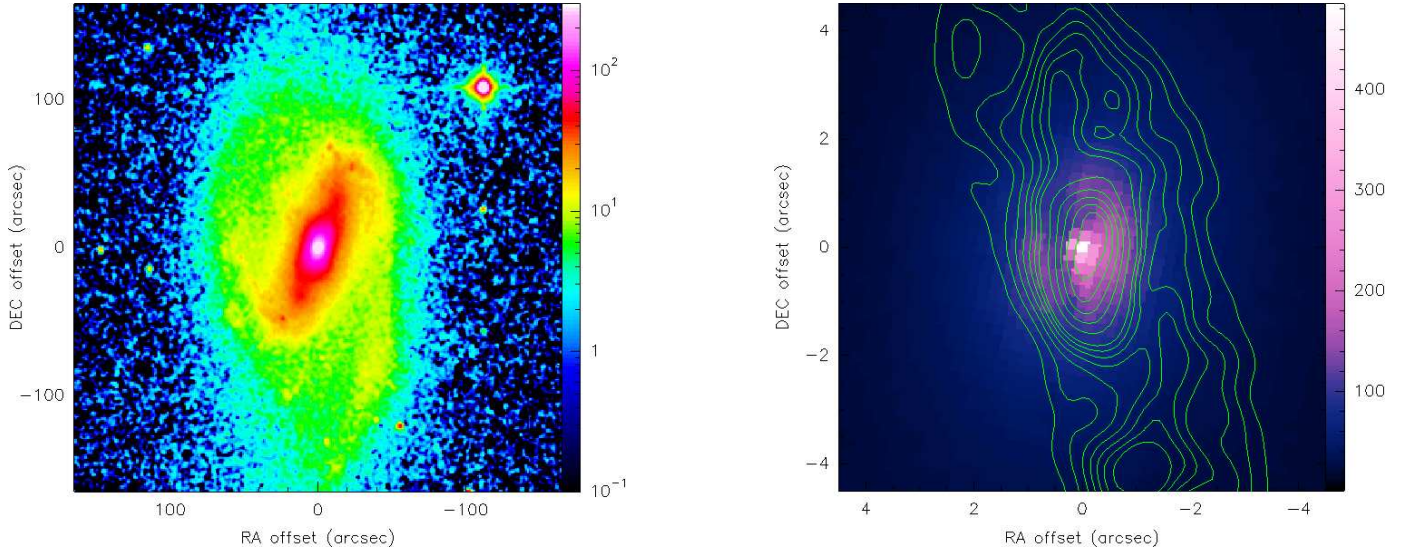


Fig. 16. *Left panel:* Large-scale H -band 2MASS image of NGC 3627 centered on the phase tracking center of our ^{12}CO interferometric observations. The inner $330''$ are shown. *Right panel:* Inner $9''$ of the F160W/ HST H -band image of NGC 3627 rotated with N up and E left and centered on the phase tracking center of our ^{12}CO interferometric observations with overlaid NUGA $^{12}\text{CO}(2-1)$ contours (in green) as in Fig. 4 (*right panel*).

trum tends to peak around $1.6\mu\text{m}$, corresponding to the H -band NIR window, $1.6\mu\text{m}$ emission is an effective tracer of stellar mass. Like the emission at $3.6\mu\text{m}$, the $1.6\mu\text{m}$ morphology of NGC 3627 is much smoother than that found at $8\mu\text{m}$ (Fig. 14); the former maps trace the older stellar population, while the latter is tracing the sites of star formation which tend to be clumpy, with a more inhomogeneous distribution. Like the

$3.6\mu\text{m}$ emission, the H -band image shows a large-scale stellar bar with $\text{PA} = -21^\circ$ and a radius of roughly $3\text{--}3.4\text{ kpc}$ ($60\text{--}70''$).

Another H -band image of NGC 3627 is available thanks to the F160W filter on the $HST/\text{NIC3}$ camera, described in Sect. 2.4. Although the smaller FOV of the NIC3 camera ($51'' \times 51''$), the superior spatial resolution of the F160W/ HST H -band image ($0''.2$), compared with that of the H -band 2MASS im-

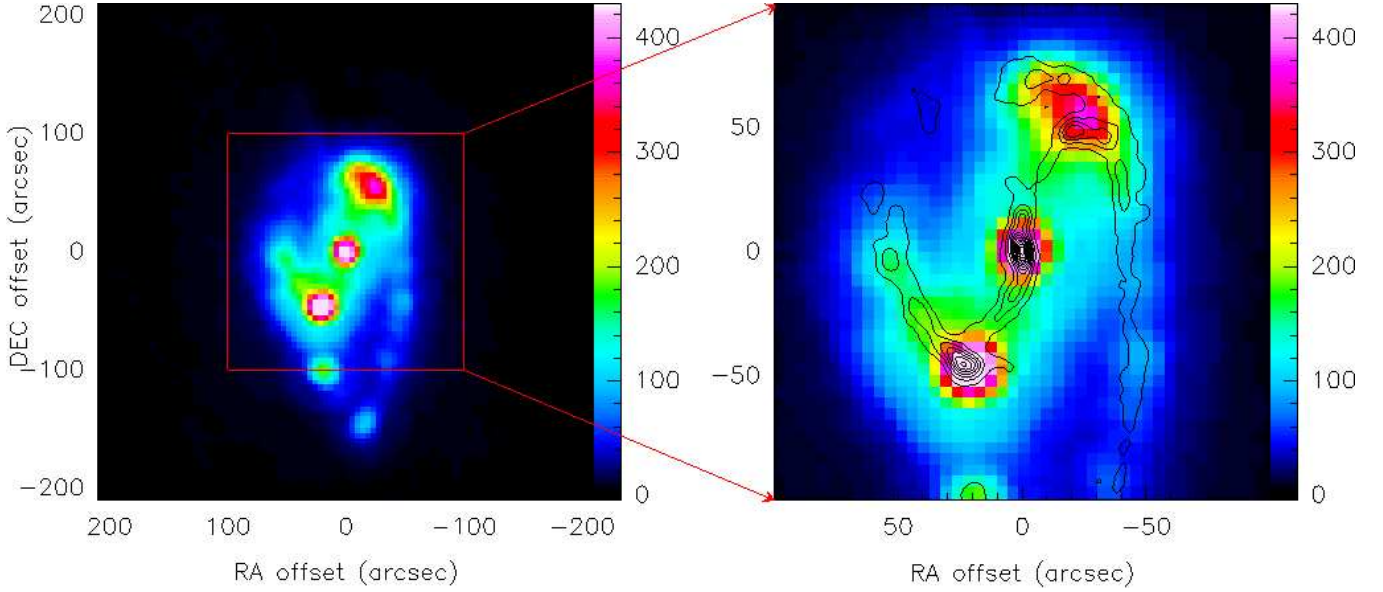


Fig. 17. *Left panel:* Large-scale *Spitzer*-MIPS $70\mu\text{m}$ image of NGC 3627, centered on the phase tracking center of our ^{12}CO interferometric observations. The inner $420''$ are shown. The (red) box shows the central $200''$, displayed in the *right panel*. *Right panel:* BIMA $^{12}\text{CO}(1-0)$ integrated intensity contours overlaid on the *Spitzer*-MIPS $70\mu\text{m}$ image of NGC 3627. The inner $200''$ are shown.

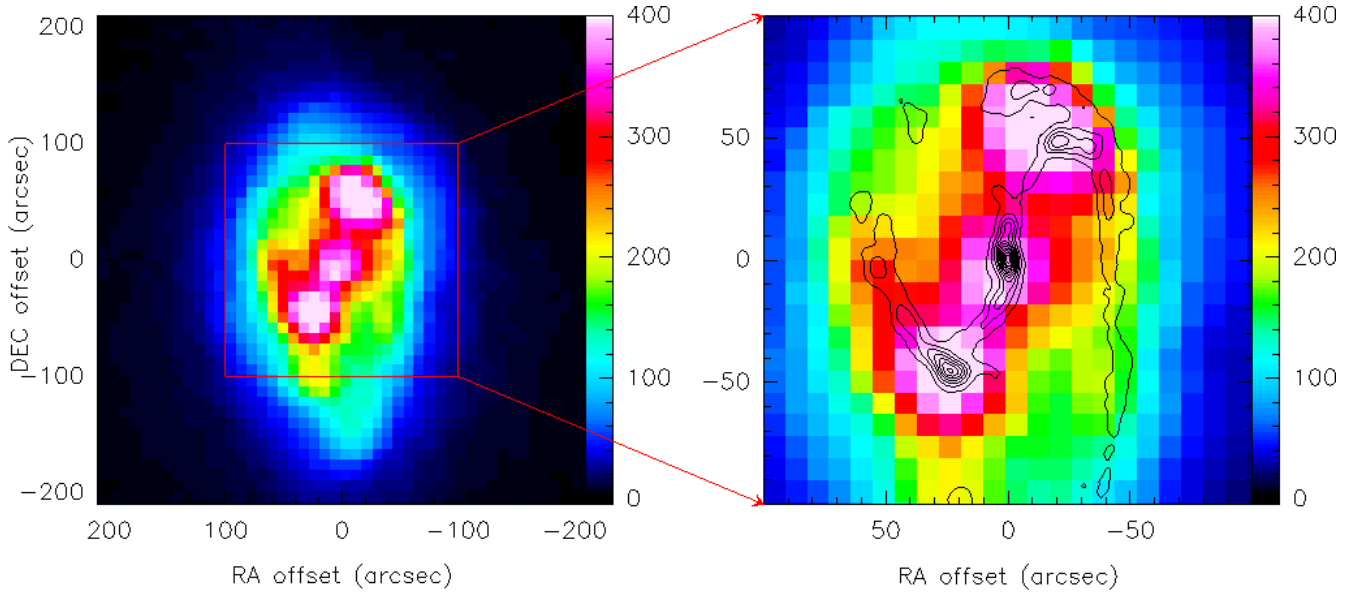


Fig. 18. *Left panel:* Large-scale *Spitzer*-MIPS $160\mu\text{m}$ image of NGC 3627, centered on the phase tracking center of our ^{12}CO interferometric observations. The inner $420''$ are shown. The (red) box shows the central $200''$, displayed in the *right panel*. *Right panel:* BIMA $^{12}\text{CO}(1-0)$ integrated intensity contours overlaid on the *Spitzer*-MIPS $160\mu\text{m}$ image of NGC 3627. The inner $200''$ are shown.

age ($2''.5$), allows to visualize more in detail the nuclear region of NGC 3627. The right panel of Fig. 16 shows the inner $9''$ of NGC 3627 of the F160W/*HST* *H*-band image with overlaid $^{12}\text{CO}(2-1)$ contours (in green) as in Fig. 4 (left panel). Although the morphology of the nuclear $^{12}\text{CO}(2-1)$ emission

is more elongated relative to the $1.6\mu\text{m}$ (F160W/*HST*) one, the sizes of the two inner ($\sim 3''$) distributions are similar and the two central peaks coincide. The central emission at $1.6\mu\text{m}$ is distributed in a disk, with a central peak and a depression toward the NE caused by dust extinction. The dust feature gives

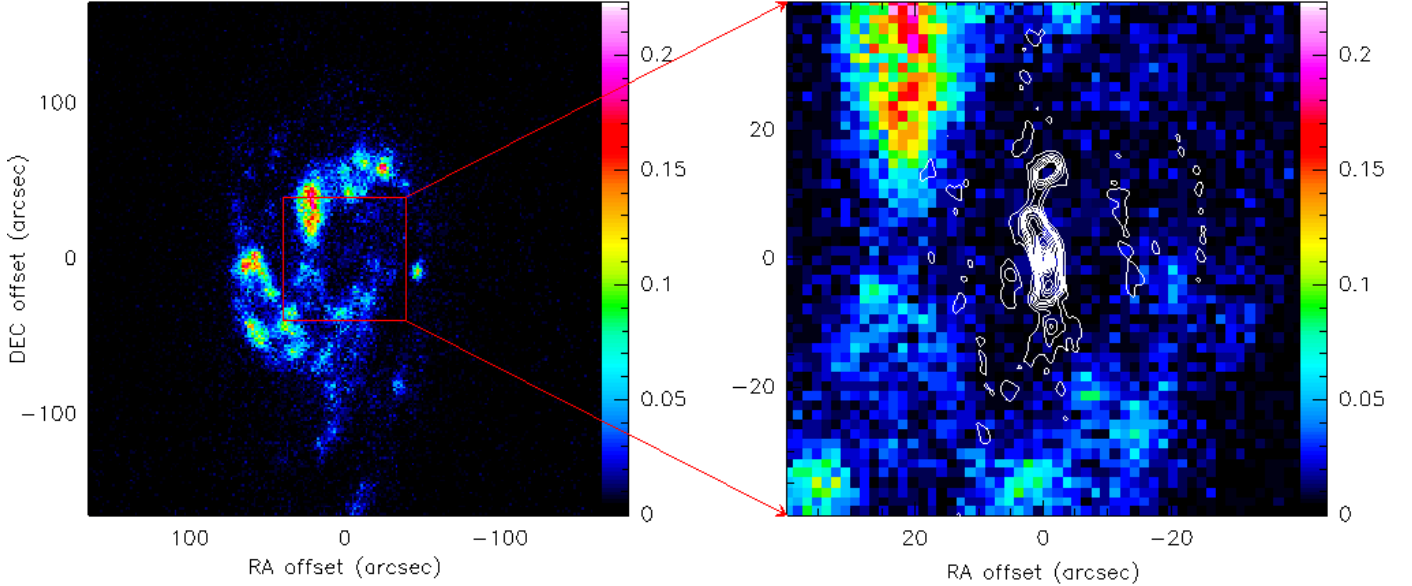


Fig. 19. *Left panel:* Large-scale *GALEX* FUV sky subtracted image of NGC 3627 centered on the phase tracking center of our ^{12}CO interferometric observations. The inner 330'' are shown. The (red) box shows the central 80'', displayed in the *right panel*. *Right panel:* $^{12}\text{CO}(1-0)$ integrated intensity contours (in white) as in Fig. 4 (*left panel*) overlaid on the *GALEX* FUV sky subtracted image of NGC 3627. The inner 80'' are shown.

a clue about the orientation of the galactic disk. Because dust on the near side of the galaxy obscures what is behind it, we can deduce that the eastern side is closer than the western side. Such an orientation would be consistent with the blue-shifted velocities toward the north (see Fig. 8), and the expectation that the spiral arms should be trailing.

5.3. Far-infrared emission

Most of the dust mass in galaxies is relatively cool, radiating primarily at wavelengths of the *Spitzer*-MIPS 70 and 160 μm bands. The left panels of Figures 17 and 18, which display the inner 420'' of the *Spitzer*-MIPS 70 and 160 μm images of NGC 3627, respectively, show that the dust emission is intensified at the nucleus and at the ansae at the ends of the bar. The right panels of these figures display the BIMA $^{12}\text{CO}(1-0)$ integrated intensity contours overlaid on the *Spitzer*-MIPS 70 μm image (Fig. 17) and the *Spitzer*-MIPS 160 μm image (Fig. 18) for the inner 200'' of NGC 3627. These comparisons show a very good correlation between the dust emission peaks and the ^{12}CO emission along the bar. These regions with strong dust and ^{12}CO emission could be the “highly obscured star-forming regions” identified by Prescott et al. (2007) by comparing 24 μm and $\text{H}\alpha$ maps. This dust-CO correlation is particularly important in terms of SF, discussed below in Sect. 5.5.

5.4. Far-ultraviolet morphology

The left panel of Figure 19 shows the FUV image of NGC 3627 obtained with the *GALEX* satellite, described in Sect. 2.4. It can

be seen that NGC 3627 has an asymmetric spiral structure in the FUV outside the range of our ^{12}CO observations, as seen at other wavelengths (IR, but also ^{12}CO from BIMA SONG survey). There is an inner elongated (north/south) ring delimiting a “hole”, or rather a net depression in the FUV emission around the nucleus. Along the edge of this ring, the FUV emission is not homogeneously distributed, but its north/northeastern arc exhibits FUV emission in the form of several clumps stronger than the rest of the ring. In the FUV, the eastern spiral arm, less extended, appears more luminous than the western one, while in the IR (8 μm [Fig. 14] and 1.6 μm [Fig. 16]) the two spiral arms are equally intense. The implication is that dust is suppressing the emission of the western arm. A similar ring is visible also in H α (Haan et al. 2008, 2009), larger than in the FUV *GALEX* emission but with the same elongated (north/south) morphology. The right panel of Fig. 19 shows our $^{12}\text{CO}(1-0)$ contours as in Fig. 4 (*left panel*) superimposed on the FUV *GALEX* image for the inner 80'' of NGC 3627. The ^{12}CO bar-like structure is contained in the inner hole observed in the FUV, indicating an anti-correlation between ^{12}CO and FUV. The same anti-correlation is observable by comparing the FUV *GALEX* image with BIMA $^{12}\text{CO}(1-0)$ contours, as displayed in Figure 20. Although the large scale views of the galaxy in FUV and $^{12}\text{CO}(1-0)$ are similar (as demonstrated by the extension of the arms, especially the western one), in Fig. 20 we can appreciate some offsets between the two emissions. Shifts between molecular gas and FUV peaks are present along both spiral arms, and the strongest FUV peak, along the ring in the north/northeast direction, has no counterpart in molecular gas emission.

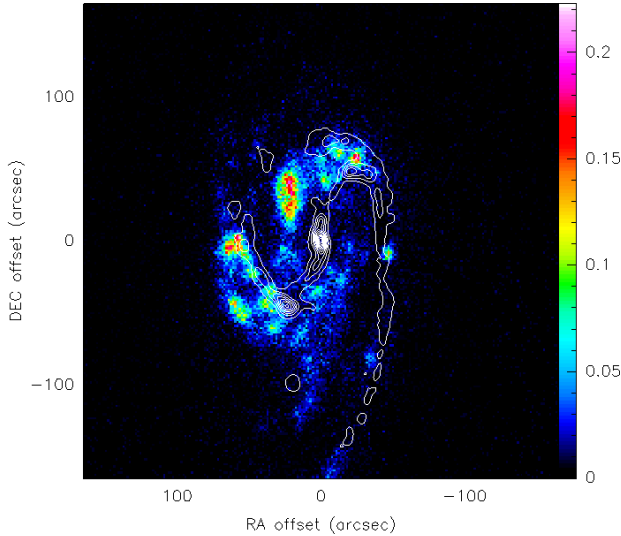


Fig. 20. BIMA $^{12}\text{CO}(1-0)$ integrated intensity contours (in white) overlaid on the *GALEX* FUV sky subtracted image of NGC 3627. The inner $320''$ are shown.

Offsets and anti-correlations between FUV and ^{12}CO (or FIR and H α) emissions have also been seen in other spiral galaxies such as M 100 (Rand 1995; Sempere & García-Burillo 1997; Calzetti et al. 2005), M 51 (Calzetti et al. 2005), and NGC 3147 (Casasola et al. 2008a). These anti-correlations may relate to star formation efficiency and timescale variations in response to a spiral density wave. The SF and its related tracers are often located in different regions of a galaxy: FUV emission is more prominent at the outer edge of the spiral arms, where typically dust extinction is low, while FIR emission is stronger at the inner edge.

The FUV-CO anti-correlation found in NGC 3627 is particularly interesting in terms of the Kennicutt-Schmidt (KS) law (Kennicutt 1998), which relates the star formation rate (SFR) density (Σ_{SFR}) to the gas surface density (Σ_{gas}). Bigiel et al. (2008) have found that at high gas surface densities, when the gas is predominantly molecular, the KS law is linear ($\Sigma_{\text{SFR}} \sim \Sigma_{\text{gas}}^N$, with $N \sim 1$) and a correlation between FUV and CO is expected. However, more than one factor may disturb the KS correlation, especially on small spatial scales. First, FUV traces older SF episodes than either H α or $24\,\mu\text{m}$ emission; hence the sites of potential future SF (as traced by CO) may be disconnected from past SF sites (FUV). Second, feedback from massive stellar winds and supernovae may disrupt the ISM on small spatial scales and degrade the KS correlation. Finally, if the molecular gas is not in dynamical equilibrium, perhaps through the action of the large-scale bar, it would not be expected to be associated with sites of current SF. The lack of correlation in the context of the KS law for this and other NUGA galaxies will be discussed in a forthcoming paper dedicated to this topic.

5.5. Star formation in NGC 3627

The FIR luminosity is often used as a measure of the current star formation rate (SFR), since it is assumed that FIR emission is mainly due to dust heating by massive young stars. The total IR luminosity of NGC 3627 is $1.3 \times 10^{44} \text{ erg s}^{-1}$, according to the precepts of Draine & Li (2007) and with fluxes from Dale et al. (2005). This corresponds to a SFR of $\sim 6 M_{\odot} \text{ yr}^{-1}$ (Kennicutt 1998). In the bulge of NGC 3627, there is little observed SF (Smith et al. 1994; Regan et al. 2002), and the SFR given by H α within a nuclear region of diameter $\sim 16''$ is $0.078 M_{\odot} \text{ yr}^{-1}$ (Regan et al. 2002), ~ 3 times lower than found in the bar itself, and ~ 4 times lower than the spiral arms (Regan et al. 2002). Part of this deficit in the nuclear H α -derived SFR may arise from dust extinction, given that the mean A_V in the inner $50''$ (diameter) is ~ 2 mag (Calzetti et al. 2007). In any case, in NGC 3627, most of the SF is extranuclear, along the bar, particularly where it terminates and the spiral arms emerge (see Figs. 17 and 18).

The $70\,\mu\text{m}$ emission is confined mainly to the nucleus and the bar, particularly the ansae (see Fig. 17). The $160\,\mu\text{m}$ emission (albeit with lower resolution), is more broadly distributed, especially around the bar. This IR morphology suggests that the dust along the bar is warmer than around the bar, probably heated by the massive stars in the recent star-formation episodes.

In galaxies with weak SF activity (e.g. NGC 4736, Smith et al. 1994), dust heating by non-OB stars may also contribute significantly (e.g., de Jong et al. 1984; Bothun et al. 1989). This more quiescent heating source may be especially important in the central regions of early/type spiral galaxies with massive bulges and little nuclear or circumnuclear SF, such as NGC 3627. The ratio of FIR to H α luminosity for the bulge of NGC 3627 is of ~ 8100 , significantly larger than for the star-forming regions in this galaxy, between ~ 1000 and ~ 2000 . The $L(\text{FIR})/L(\text{H}\alpha)$ ratio is also higher than can be accounted for by obscured SF with a normal initial mass function, using extinction measurements derived from $^{12}\text{CO}(1-0)$ and FIR data (Smith et al. 1994). Thus, the older stars probably contribute significantly to the dust heating in the bulge of NGC 3627 (Smith et al. 1994).

A low nuclear SFR is consistent with the CO/HCN ratio (10) discussed in Sect. 3. Higher ratios suggest that excitation by SF is dominant over AGN excitation in the circumnuclear region, but we found a “normal” CO/HCN ratio for NGC 3627, not surprisingly given its low SFR.

6. Computation of the torques on the molecular gas

The gravitational torques derived from the stellar potential in the inner region of NGC 3627 allow to account for the gas kinematics derived from CO and examine the efficiency of gravitational torques exerted on the gas. As described in previous NUGA papers (e.g., García-Burillo et al. 2005), to compute the gravitational torques we assume that NIR images give the best approximation for the total stellar mass distribution, being less

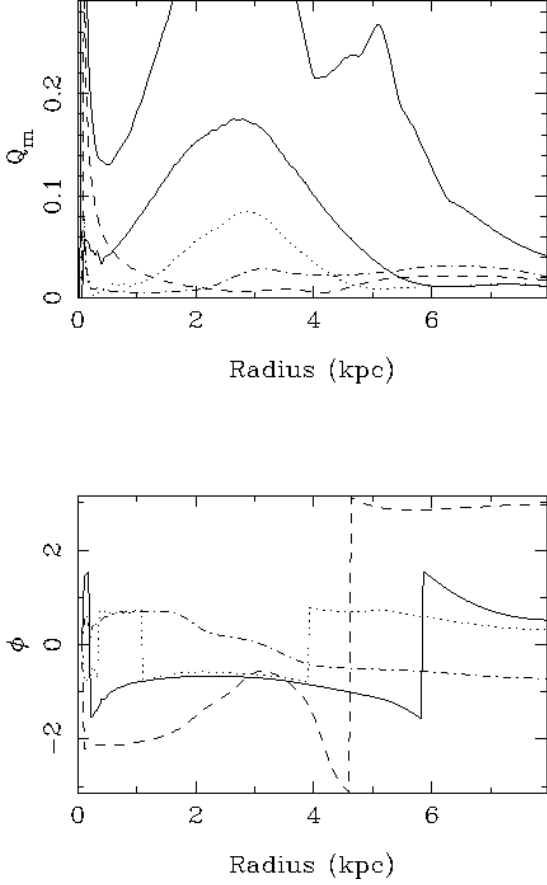


Fig. 21. The strength Q (top) and phase Φ (bottom) of the $m = 1, 2, 3, 4$ Fourier components of the potential, derived from the *Spitzer*-IRAC 3.6 μm image. The full lines correspond to $m = 2$ and the total strength, the dashed line to $m = 1$, dot-dash to $m = 3$, and dots to $m = 4$.

affected than optical images by dust extinction or stellar population bias.

6.1. Evaluation of the gravitational potential

We computed the torques using both *HST*-NICMOS F160W and *Spitzer*-IRAC 3.6 μm images. They yield complementary results, the torques computed from the *HST*-NICMOS F160W image compared with the ^{12}CO PdBI contours allow to investigate the nuclear region of NGC 3627, while the torques derived from the *Spitzer*-IRAC image in combination with the ^{12}CO BIMA contours are much better adapted to visualize the whole spiral structure of the galaxy. We perform the subtraction of foreground stars, deprojection, and resampling, as described in other NUGA papers (e.g., García-Burillo et al. 2005).

Here, we briefly recall some definitions and assumptions used to evaluate the gravitational torques. NIR images are completed in the vertical dimension by assuming an isothermal plane model with a constant scale height, equal to $\sim 1/12$ th of the radial scale-length of images. With a Fourier transform

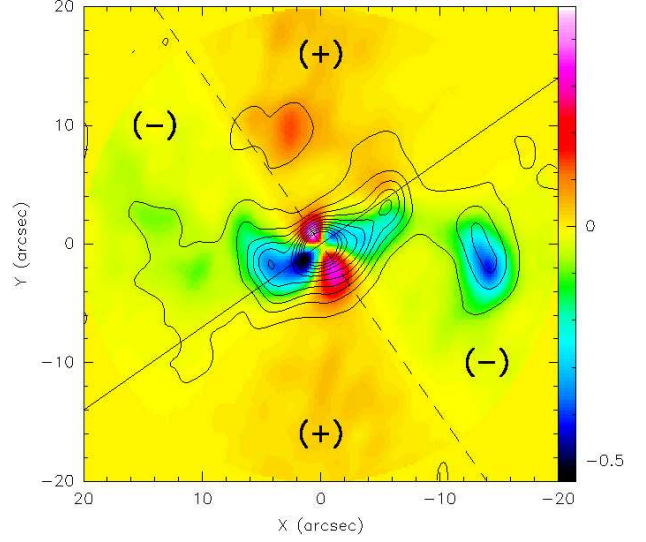


Fig. 22. NUGA PdBI $^{12}\text{CO}(1-0)$ contours are overlaid onto the gravitational torque map computed from the *HST*-NICMOS F160W image ($t(x,y) \times \Sigma(x,y)$, as defined in text) in the center of NGC 3627. The map is deprojected, and rotated so that the major axis of the galaxy is oriented parallel to the abscissa Ox . The continuum line is oriented along the large-scale bar in the plane of the galaxy ($\text{PA} = 35^\circ$), the dashed one orthogonally to the continuum line. The quadrants labeled with (+) refer to positive torques, while those labeled with (-) to negative torques. The derived torques change sign as expected in a *butterfly* diagram.

method we derive the potential and we assume a constant mass-to-light (M/L) ratio able to reproduce the observed ^{12}CO RCs. Beyond a radius of $20''$ (or 1.96 kpc in diameter), the mass density is set to 0 in the *HST*-NICMOS F160W image, thus suppressing any spurious $m = 4$ terms. This assumption is sufficient to compute the potential over the PdBI $^{12}\text{CO}(1-0)$ primary beam. For the *Spitzer*-IRAC 3.6 μm image, this radius truncation is done at $169''$ (or 16.6 kpc in diameter).

For the non-axisymmetric part of the potential $\Phi(R, \theta)$, we decompose $\Phi(R, \theta)$ in Fourier components (m -modes), following Combes & Sanders (1981):

$$\Phi(R, \theta) = \Phi_0(R) + \sum_{m=1}^{\infty} \Phi_m(R) \cos[m\theta - \phi_m(R)]$$

where $\Phi_m(R)$ and $\phi_m(R)$ are the amplitude and phase of the m -mode, respectively.

The strength of each m -Fourier component, $Q_m(R)$, is defined by the ratio between tangential and radial forces, $Q_m(R) = m\Phi_m(R)/R|F_0(R)|$. The strength of the total non-axisymmetric perturbation is defined by:

$$Q_T(R) = \frac{F_T^{\max}(R)}{F_0(R)}$$

where $F_T^{\max}(R)$ and $F_0(R)$ represent the maximum amplitude of the tangential force and the mean axisymmetric radial force,

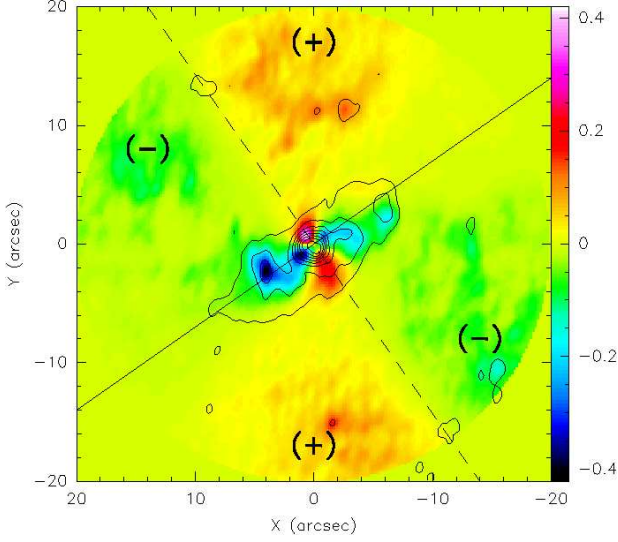


Fig. 23. Same as Fig. 22 for our NUGA PdBI $^{12}\text{CO}(2-1)$ emission taken as tracer of gas surface density.

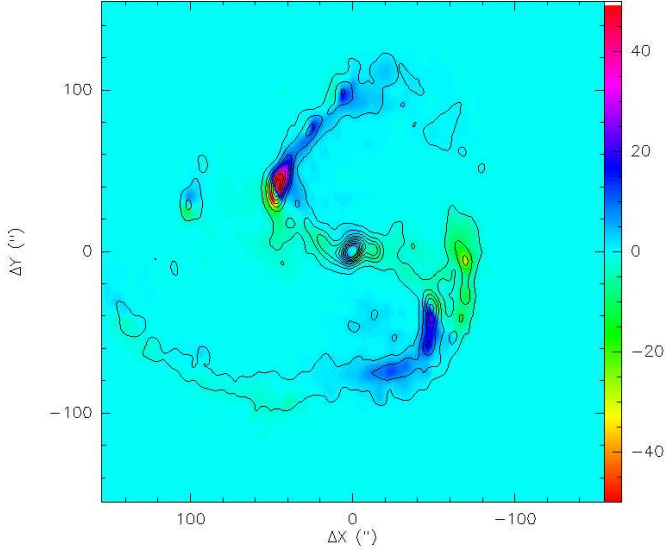


Fig. 24. The BIMA $^{12}\text{CO}(1-0)$ contours are overlaid onto the gravitational torque map computed from the *Spitzer*-IRAC $3.6\ \mu\text{m}$ image. As for Fig. 22, the torque map (color scale) is plotted on a symmetric palette (wedge), and is deprojected and rotated so that the major axis of the galaxy is oriented parallel to the abscissa Ox .

respectively. Figure 21 shows the strengths (top panel) and phases (bottom panel) vs. radius for the *Spitzer*-IRAC $3.6\ \mu\text{m}$ image and for the first m components.

6.2. Evaluation of the gravity torques

The forces per unit mass (F_x and F_y), obtained from the derivatives of $\Phi(R, \theta)$ on each pixel, allow to compute the torques per unit mass $t(x, y)$ by:

$$t(x, y) = x F_y - y F_x.$$

The torque map is oriented according to the sense of rotation in the plane of the galaxy. The combination of the torque map and the gas density Σ map allows to derive the net effect on the gas at each radius. Figures 22 and 23 show gravitational torque maps, computed from the *HST*-NICMOS F160W image, weighted by the gas surface density $t(x, y) \times \Sigma(x, y)$, normalized to their maximum value, for NUGA PdBI $^{12}\text{CO}(1-0)$ and $^{12}\text{CO}(2-1)$, respectively. The difference in orientation between the large-scale bar and the major axis of the galaxy ($\sim 19^\circ$ in the sky plane) implies that the deprojected difference in PAs is $\sim 35^\circ$. In both figures, the continuum line is oriented along the large-scale bar in the plane of the galaxy ($\text{PA} = 35^\circ$), the dashed one orthogonally to the continuum line. In the two quadrants labeled with (+) the torques are positive, while in those labeled with (-) the torques are negative. The derived torques change sign following a characteristic 2D *butterfly* pattern produced by the bar. Figure 24 shows the gravitational torque map, derived from the *Spitzer*-IRAC $3.6\ \mu\text{m}$ image, weighted by the gas surface density $t(x, y) \times \Sigma(x, y)$, normalized to their maximum value, for BIMA $^{12}\text{CO}(1-0)$. The observed gas distribution is representative of the time spent by a molecular cloud on a typical orbit at this location.

By using $\Sigma(x, y)$ as the actual weighting function, we first compute the torque per unit mass averaged over azimuth:

$$t(R) = \frac{\int_{\theta} \Sigma(x, y) \times (x F_y - y F_x)}{\int_{\theta} \Sigma(x, y)}$$

where $t(R)$ is, for definition, the time derivative of the specific angular momentum L of the gas averaged azimuthally, $t(R) = dL/dt|_{\theta}$. Then, to have dimensionless quantities, we normalize this variation of angular momentum per unit time to the angular momentum at this radius and to the rotation period. Finally, we estimate the efficiency of the gas flow as the average fraction of the gas specific angular momentum transferred in one rotation (T_{rot}) by the stellar potential, as a function of radius:

$$\frac{\Delta L}{L} = \frac{dL}{dt} \bigg|_{\theta} \times \frac{1}{L} \bigg|_{\theta} \times T_{rot} = \frac{t(R)}{L_{\theta}} \times T_{rot}$$

where L_{θ} is assumed to be well represented by its axisymmetric estimate, $L_{\theta} = R \times v_{rot}$. Figures 25 show $\Delta L/L$ curves computed with the *HST*-NICMOS F160W image for NGC 3627 derived from the PdBI $^{12}\text{CO}(1-0)$ [left] and the $^{12}\text{CO}(2-1)$ [right] data. The (red) dashed area corresponds to the resolution limit of our observations. In the left panel, the $^{12}\text{CO}(1-0)$ map resolution is ~ 125 pc, while in the right panel the $^{12}\text{CO}(2-1)$ map resolution is ~ 59 pc. In the right panel, the (green) vertical dashed line at 0.51 kpc indicates the $^{12}\text{CO}(2-1)$ FOV at the PdBI. These figures show that the torques are negative within the inner 0.4 kpc,

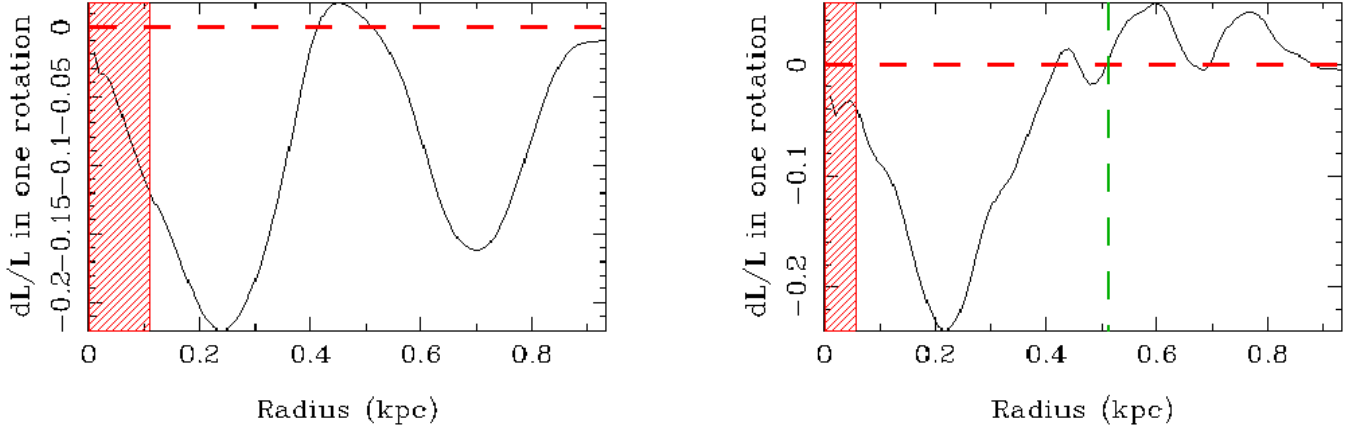


Fig. 25. The torque, or more precisely the fraction of the angular momentum transferred from/to the gas in one rotation (dL/L), computed with the *HST*-NICMOS F160W image, is plotted for $^{12}\text{CO}(1-0)$ [left] and $^{12}\text{CO}(2-1)$ [right]. The (red) dashed area corresponds to the resolution limit of our observations. In the left panel, the limiting factor is the $^{12}\text{CO}(1-0)$ map resolution (~ 125 pc), while, on the right, the $^{12}\text{CO}(2-1)$ map resolution (~ 59 pc). In the right panel, the (green) vertical dashed line at 0.51 kpc indicates the $^{12}\text{CO}(2-1)$ FOV at the PdBI.

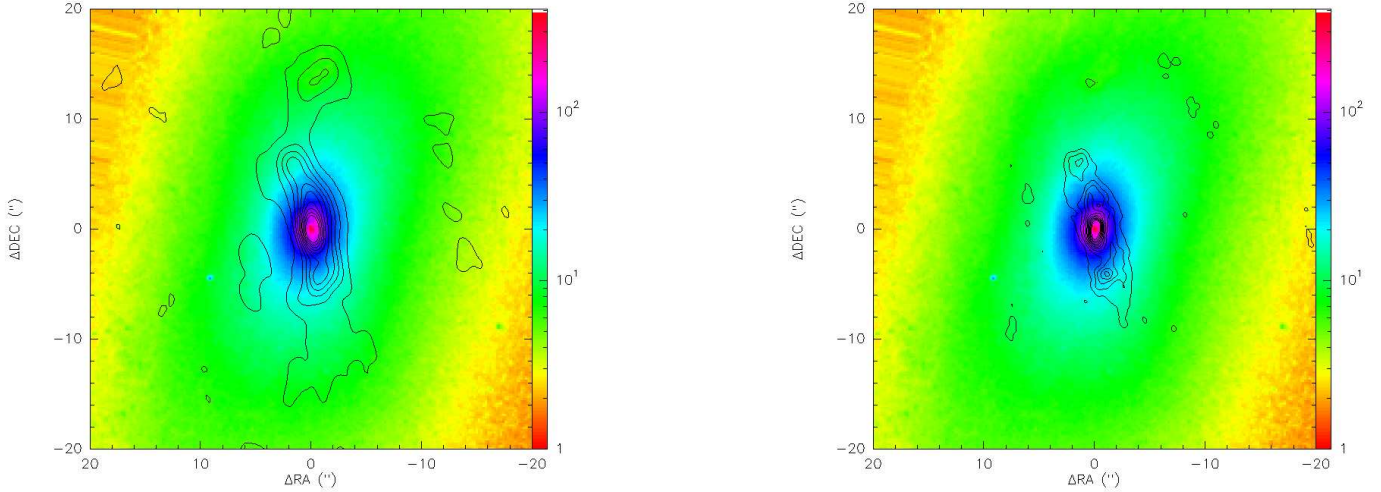


Fig. 26. *Left panel:* Our NUGA PdBI $^{12}\text{CO}(1-0)$ contours overlaid on the *HST*-NICMOS F160W image of NGC 3627 in false color. The inner $40''$ are shown. *Right panel:* Same as left panel but for the $^{12}\text{CO}(2-1)$ line.

down to the resolution limit of our observations, and reach a (negative) peak at 0.2 kpc for both $^{12}\text{CO}(1-0)$ and $^{12}\text{CO}(2-1)$. For $^{12}\text{CO}(1-0)$, they oscillate and become negative again at 700 pc. This second (negative) peak is not present in $^{12}\text{CO}(2-1)$, because it is outside the $^{12}\text{CO}(2-1)$ FOV. Figures 26 show NUGA PdBI $^{12}\text{CO}(1-0)$ [left] and the $^{12}\text{CO}(2-1)$ [right] contours overlaid on the *HST*-NICMOS F160W image. This figure clearly shows that the gas is leading the bar (the sense of the rotation is direct) since the PA of the bar is -21° , while the bulk emission of the molecular gas is distributed along a bar-like structure with a PA of 14° for the $^{12}\text{CO}(1-0)$ line and of 15° for

the $^{12}\text{CO}(2-1)$ one (see Fig. 8 and Sect. 4.4). This explains the negative torques observed in Figs. 25.

Figure 27 shows the large-scale $\Delta L/L$ curves computed with the *Spitzer*-IRAC $3.6 \mu\text{m}$ image and the BIMA-SONG images. The (blue) dashed area corresponds to the resolution limit of BIMA observations, ~ 670 pc. In this figure, the torques are negative within the inner ~ 3 kpc, down to the resolution limit of BIMA maps, and positive at larger radii. Resonances in barred galaxies are related to the pattern speed of the stellar bar, which can be inferred from the angular velocity at the corotation (CR) radius. In early-type barred galaxies, CR is lo-

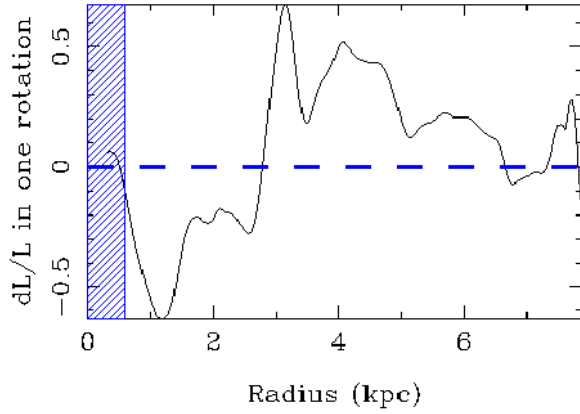


Fig. 27. The torque, or more precisely the fraction of the angular momentum transferred from/to the gas in one rotation (dL/L), computed with the *Spitzer*-IRAC 3.6 μm image, is plotted for BIMA $^{12}\text{CO}(1-0)$ observations. The (blue) dashed area corresponds to the resolution limit of the BIMA observations (~ 670 pc).

cated near the end of the bar between $R = R_{\text{bar}}$ and $R = 1.4R_{\text{bar}}$ (Elmegreen 1996). As said before, in NGC 3627, the torques are negative within the inner ~ 3 kpc, and the radius of ~ 3 kpc would correspond to the end of the bar, or to the CR radius estimated by Chemin et al. (2003) between 2.6 and 3.7 kpc. The large-scale gas response inside the bar is twisted, i.e., the gas appears along the bar leading edges (see Fig. 4). This is due to the dissipation there where the torques act, and it is a scenario which does not require any inner Lindblad resonance (ILR). In any case, the PdBI-based torques from the NICMOS image (Fig. 25) are more reliable in the center than the ones inferred from BIMA observations and the IRAC image (Fig. 27) because of the higher spatial resolution of the PdBI+NICMOS.

7. Dynamical interpretation

Figure 28 shows the model RC (V_{rot}) obtained from the *Spitzer*-IRAC 3.6 μm image, and the derived frequencies Ω , $\Omega - k/2$, and $\Omega + k/2$ for NGC 3627. We have also derived a model RC from the *HST*-NICMOS F160W image, which is identical to the model RC from the *Spitzer*-IRAC 3.6 μm image until 1.3 kpc from the center (it is not shown in the figure because it adds no new information). The model RC has been calibrated to the $\text{H}\alpha$ RC derived from Chemin et al. (2003), to have $V = 212 \text{ km s}^{-1}$ at 8 kpc. Fig. 28 shows that if the stellar bar ends at ~ 3 kpc (blue vertical line), with a pattern speed of the bar $\Omega_p \sim 65 \text{ km s}^{-1} \text{ kpc}^{-1}$ (blue horizontal line) then the CR of the bar would be at ~ 3.3 kpc, consistent with the results of Chemin et al. (2003) who estimated the CR radius between 2.6 and 3.7 kpc. The $\Omega - k/2$ curve could be marginally compatible with an ILR at $r = 500$ pc, but because there is no clear ring signature in the morphology, we exclude the presence of

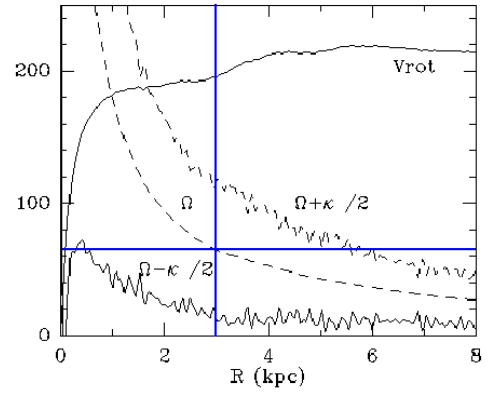


Fig. 28. Model rotation curve V_{rot} (in km s^{-1}) and derived frequencies Ω , $\Omega - k/2$, and $\Omega + k/2$ (in $\text{km s}^{-1} \text{ kpc}^{-1}$) for NGC 3627. The (blue) vertical line indicates the stellar bar end (~ 3 kpc), while the (blue) horizontal one indicates the pattern speed of the bar at $\Omega_p \sim 65 \text{ km s}^{-1} \text{ kpc}^{-1}$.

an ILR. In addition, since there is a strong bar, true precessing rate is lower than the epicyclic approximation $\Omega - k/2$ curve, and therefore the curve is only an upper limit. Hence there is probably no ILR. The absence of an ILR was already discussed in Sect. 6.2, where we elaborated such a scenario.

The pattern speed of NGC 3627 has been measured by several authors. Chemin et al. (2003) have assumed that the inner ring-like feature found by Regan et al. (2002) but not by us, corresponds to the location of an ultra-harmonic resonance. Rand & Wallin (2004), using the BIMA SONG data and the Tremaine-Weinberg method, have measured a pattern speed of the bar of $\Omega_p = 50^{+3}_{-8} \text{ km s}^{-1} \text{ kpc}^{-1}$, in good agreement with our determination.

In the presence of an ILR, the torques should be negative between the CR of the bar and the ILR. For NGC 3627, without an ILR, the torques are negative between the CR of the bar and the AGN, down to the resolution limit of our observations. Such a conclusion would be the natural outcome of a scenario in which a young and rapidly rotating bar has had no time to slow down due to secular evolution, and has not yet formed any ILR. The presence of molecular gas inside the ILR of the primary bar, or where we expect that the ILR will form, makes NGC 3627 a potential *smoking gun* of inner gas inflow. In this scenario, the gas there is certainly fueling the central region, and in a second step could fuel directly the AGN. Finding *smoking gun* evidence of AGN fueling is proving to be quite challenging, perhaps because of the short-lived nature of the mechanisms responsible.

8. Summary and conclusions

The molecular gas, traced by $^{12}\text{CO}(1-0)$ and $^{12}\text{CO}(2-1)$ transitions, in the interacting barred LINER/Seyfert 2 galaxy NGC 3627 is distributed along a bar-like structure of $\sim 18''$

(~ 900 pc) diameter ($PA = 14^\circ$) with two peaks at the extremes. The $1.6\mu\text{m}$ *H*-band 2MASS and $3.6\mu\text{m}$ *Spitzer*-IRAC images of NGC 3627 show a stellar bar in the nucleus with $PA = -21^\circ$, different from the $PA (= 14^\circ)$ of the molecular gas bar-like structure, suggesting that the gas is leading the stellar bar. Instead, the *GALEX* FUV emission of NGC 3627 displays an inner elongated (north/south) ring delimiting a hole around the nucleus and containing the $^{12}\text{CO} \sim 18''$ bar-like structure. This kind of anti-correlation between FUV, molecular gas, and the stellar bar is perhaps related to star formation efficiency and timescale variations in response to a spiral density wave. The gravity torques exerted by the stellar potential on the gas computed with the *HST*-NICMOS F160W image and our PdBI maps are negative within the inner 0.4 kpc, down to the resolution limit of our observations.

The torques computed with the *Spitzer*-IRAC $3.6\mu\text{m}$ image and BIMA ^{12}CO map (with a resolution limit of ~ 670 pc) are also negative within the inner ~ 3 kpc. If the bar ends at ~ 3 kpc, with a pattern speed of the bar $\Omega_p \sim 65 \text{ km s}^{-1} \text{ kpc}^{-1}$ then the CR of the bar would be at ~ 3.3 kpc. There is no clear ring signature and we thus exclude the presence of an ILR. Without an ILR, the torques are negative between the CR of the bar and the AGN, down to the resolution limit of our observations. This scenario is compatible with a young/incipient bar which had no time to slow down from secular evolution, and has not yet formed any ILR. NGC 3627 is a potential *smoking gun* of inner gas inflow: the gas is certainly fueling the central region, and in a second step could fuel directly the AGN.

NGC 3627 is the fifth *smoking gun* NUGA galaxy, together with NGC 6574 (Lindt-Krieg et al. 2008), NGC 2782 (Hunt et al. 2008), NGC 3147 (Casasola et al. 2008a), and NGC 4579 (García-Burillo et al. 2009). The common feature shared by these galaxies is a slowly rotating stellar bar (or oval) with overlapping dynamical resonances (Casasola et al. 2008b) associated with kinematically decoupled inner bars or ovals. Such resonances and kinematic decoupling are fostered by a large central mass concentration and high gas fraction. NGC 3627 is the unique potential *smoking gun* NUGA galaxy with only one slowly rotating stellar bar. For NGC 3627, this drives a molecular bar-like structure, apparently sufficient to transport the gas toward the AGN that, in a second step, could fuel directly the active nucleus.

Acknowledgements. The authors would like to thank the referee, Greg Bothun, whose comments have been very useful for improving the original version of the paper. We thank the scientific and technical staff at IRAM for their work in making our 30 m and PdBI observations possible. This research has made use of the NASA/IPAC Extragalactic Database (NED), HyperLeda Database, *IRAS* Catalog, *Spitzer* archive, and *MAST/GALEX* images.

References

- Beauvais, C., & Bothun, G. 1999, *ApJS*, 125, 99
 Bigiel, F., Leroy, A., Walter, F., Brinks, E., de Blok, W. J. G., Madore, B., & Thornley, M. D. 2008, *AJ*, 136, 2846
 Böker, T., et al. 1999, *ApJS*, 124, 95

- Boone, F., et al. 2007, *A&A*, 471, 113 (NUGA VII)
 Bothun, G. D., Lonsdale, C. J., & Rice, W. 1989, *ApJ*, 341, 129
 Braine, J., & Combes, F. 1992, *A&A*, 264, 433
 Calzetti, D., et al. 2005, *ApJ*, 633, 871
 Calzetti, D., et al. 2007, *ApJ*, 666, 870
 Casasola, V., Bettoni, D., & Galletta, G. 2004, *A&A*, 422, 941
 Casasola, V., Combes, F., García-Burillo, S., Hunt, L. K., León, S., & Baker, A. J. 2008a, *A&A*, 490, 61 (NUGA X)
 Casasola, V., et al. 2008b, “Tumbling, Twisting, and Winding Galaxies: Pattern Speeds along the Hubble Sequence” Conference, Padova, August 25-28, 2008, *Memorie della Società Astronomica Italiana*, arXiv:0811.1971
 Casasola, V., Hunt, L. K., Combes, F., García-Burillo, S., Boone, F., Eckart, A., Neri, R., & Schinnerer, E. 2010, *A&A*, 510, A52 (NUGA XIII)
 Chemin, L., Cayatte, V., Balkowski, C., Marcelin, M., Amram, P., van Driel, W., & Flores, H. 2003, *A&A*, 405, 89
 Combes, F., & Sanders, R. H. 1981, *A&A*, 96, 164
 Combes, F., & Gerin, M. 1985, *A&A*, 150, 327
 Combes, F., et al. 2004, *A&A*, 414, 857 (NUGA II)
 Combes, F., et al. 2009, *A&A*, 503, 73 (NUGA XII)
 Dahlem, M., Heckman, T. M., Fabbiano, G., Lehnert, M. D., & Gilmore, D. 1996, *ApJ*, 461, 724
 Dale, D. A., et al. 2005, *ApJ*, 633, 857
 de Jong, T., Clegg, P. E., Rowan-Robinson, M., Soifer, B. T., Habing, H. J., Houck, J. R., Aumann, H. H., & Raimond, E. 1984, *ApJ*, 278, L67
 Draine, B. T., & Li, A. 2007, *ApJ*, 657, 810
 Elmegreen, B. 1996, *IAU Colloq. 157: Barred Galaxies*, 91, 197
 Ferrarese, L., Pogge, R. W., Peterson, B. M., Merritt, D., Wandel, A., & Joseph, C. L. 2001, *ApJ*, 555, L79
 Filho, M. E., Barthel, P. D., & Ho, L. C. 2000, *ApJS*, 129, 93
 Gao, Y., & Solomon, P. M. 2004, *ApJS*, 152, 63
 García-Burillo, S., Guélin, M., & Cernicharo, J. 1993, *A&A*, 274, 123
 García-Burillo, S., et al. 2003, *A&A*, 407, 485 (NUGA I)
 García-Burillo, S., Combes, F., Schinnerer, E., Boone, F., & Hunt, L. K. 2005, *A&A*, 441, 1011 (NUGA IV)
 García-Burillo, S., et al. 2009, *A&A*, 496, 85 (NUGA XI)
 Gil de Paz, A., et al. 2007, *ApJS*, 173, 185
 Guilloteau, S., & Lucas, R. 2000, *Imaging at Radio through Submillimeter Wavelengths*, 217, 299
 Haan, S., Schinnerer, E., Mundell, C. G., García-Burillo, S., & Combes, F. 2008, *AJ*, 135, 232
 Haan, S., Schinnerer, E., Emsellem, E., García-Burillo, S., Combes, F., Mundell, C. G., & Rix, H.-W. 2009, *ApJ*, 692, 1623
 Haynes, M. P., Giovanelli, R., & Roberts, M. S. 1979, *ApJ*, 229, 83
 Heckman, T. M., Kauffmann, G., Brinchmann, J., Charlot, S., Tremonti, C., & White, S. D. M. 2004, *ApJ*, 613, 109
 Helfer, T. T., Thornley, M. D., Regan, M. W., Wong, T., Sheth, K., Vogel, S. N., Blitz, L., & Bock, D. C.-J. 2003, *ApJS*, 145, 259

- Ho, L. C., Filippenko, A. V., & Sargent, W. L. W. 1997, *ApJS*, 112, 315
- Hopkins, P. F., & Hernquist, L. 2006, *ApJS*, 166, 1
- Hunt, L. K., et al. 2008, *A&A*, 482, 133 (NUGA IX)
- Janiuk, A., Czerny, B., Siemiginowska, A., & Szczerba, R. 2004, *ApJ*, 602, 595
- Jogee, S., Scoville, N., & Kenney, J. D. P. 2005, *ApJ*, 630, 837
- Kennicutt, R. C., Jr. 1998, *ARA&A*, 36, 189
- Kennicutt, R. C., Jr., et al. 2003, *PASP*, 115, 928
- King, A. R., & Pringle, J. E. 2007, *MNRAS*, 377, L25
- Knapen, J. H., Pérez-Ramírez, D., & Laine, S. 2002, *MNRAS*, 337, 808
- Krips, M., et al. 2005, *A&A*, 442, 479 (NUGA III)
- Krips, M., et al. 2007, *A&A*, 468, L63
- Krips, M., Neri, R., García-Burillo, S., Martín, S., Combes, F., Graciá-Carpio, J., & Eckart, A. 2008, *ApJ*, 677, 262
- Kuno, N., et al. 2007, *PASJ*, 59, 117
- Lindt-Krieg, E., Eckart, A., Neri, R., Krips, M., Pott, J.-U., García-Burillo, S., & Combes, F. 2008, *A&A*, 479, 377 (NUGA VIII)
- Marecki, A., Spencer, R. E., & Kunert, M. 2003, *Publications of the Astronomical Society of Australia*, 20, 46
- Mulchaey, J. S., & Regan, M. W. 1997, *ApJ*, 482, L135
- Nagar, N. M., Falcke, H., Wilson, A. S., & Ho, L. C. 2000, *ApJ*, 542, 186
- Paladino, R., Murgia, M., Tarchi, A., Moscadelli, L., & Comito, C. 2008, *A&A*, 485, 679
- Paturel, G., Petit, C., Prugniel, P., Theureau, G., Rousseau, J., Brouty, M., Dubois, P., & Cambrésy, L. 2003, *A&A*, 412, 45
- Prescott, M. K. M., et al. 2007, *ApJ*, 668, 182
- Ptak, A., Colbert, E., van der Marel, R. P., Roye, E., Heckman, T., & Towne, B. 2006, *ApJS*, 166, 154
- Rand, R. J. 1995, *AJ*, 109, 2444
- Rand, R. J., & Wallin, J. F. 2004, *ApJ*, 614, 142
- Regan, M. W., Thornley, M. D., Helfer, T. T., Sheth, K., Wong, T., Vogel, S. N., Blitz, L., & Bock, D. C.-J. 2001, *ApJ*, 561, 218
- Regan, M. W., Sheth, K., Teuben, P. J., & Vogel, S. N. 2002, *ApJ*, 574, 126
- Rubin, V. C., Kenney, J. D. P., & Young, J. S. 1997, *AJ*, 113, 1250
- Sakamoto, K., Okumura, S. K., Ishizuki, S., & Scoville, N. Z. 1999, *ApJ*, 525, 691
- Sempere, M. J., & Garcia-Burillo, S. 1997, *A&A*, 325, 769
- Smith, B. J., Harvey, P. M., Colome, C., Zhang, C. Y., DiFrancesco, J., & Pogge, R. W. 1994, *ApJ*, 425, 91
- Solomon, P. M., & Barrett, J. W. 1991, *Dynamics of Galaxies and Their Molecular Cloud Distributions*, 146, 235
- Walter, F., Brinks, E., de Blok, W. J. G., Bigiel, F., Kennicutt, R. C., Thornley, M. D., & Leroy, A. 2008, *AJ*, 136, 2563
- Welch, W. J., et al. 1996, *PASP*, 108, 93
- Young, J. S., et al. 1995, *ApJS*, 98, 219
- Zhang, X., Wright, M., & Alexander, P. 1993, *ApJ*, 418, 100
- Zwicky, F. 1956, *PASP*, 68, 121